University of Padova

Department of Physics and Astronomy "Galileo Galilei"

Master Thesis in Astrophysics and Cosmology

EFFECTS OF DIFFUSION AND BACK-REACTION ON THE FORMATION OF A GAP IN THE DUST AROUND A PLANET EMBEDDED IN A CIRCUMSTELLAR DISK

Supervisor
Prof. Francesco Marzari

Candidate
Athos Ribeiro da Silva

Academic Year
2021/2022

Abstract

The life of a disk that holds two Jupiter-like planets is usually marked by the appearance of a gap. Given the disk properties, the planetary pair will follow into an inward convergent orbit, and at some point, they will establish a resonance ratio between their orbital periods, then revert the direction of motion to an outward migration. A pressure maximum will be built at the outer edge of the common gap that, if it works efficiently, will block the dust from falling and being accreted by the star, providing a good environment for dust evolution. The dust gap will keep up increasing in size while the gaseous one will maintain shape, only shifting its position outwards.

In this dissertation, we propose the execution of a two-dimensional, high-resolution hydrodynamical simulation that reproduces the circumstances described above. We apply the FARGO3D code with a multi-fluid implementation which introduces different populations of dust particle size along with the gas. Our aim is to include the effects of turbulent motion from the gas and the back-reaction of the dust on the gaseous component, in order to ascertain the impacts of both interactions on the gap formation.

We found that this addition can affect the dust trap according to particle size (up to 1 mm), promoting a dust species filtration between the outer and inner disks. Nevertheless, it does not interfere significantly with the formation of the over-density.

Contents

1

Introduction

Circumstellar disks play an important role in planetary formation since there is strong evidence that they are the cradle of planetary systems. The disks, in particular those observed by ALMA, are not homogeneous entities but often present gaps, spirals, and internal holes. Different mechanisms may be responsible for these features like the presence of a companion star, photoevaporation, and planet formation.

In this thesis, we will focus on giant planet evolution and its effects on the dust distribution of the disk. In particular, the scenario with two giant planets being trapped in resonance and migrating outwards. Marzari et al [1] performed two-dimensional hydrodynamical simulations modeling the evolution of gas and dust in a circumstellar disk with two planets similar to Jupiter and Saturn. In the proximity of the planets, a common gap develops where the gas has a significantly lower density. At the borders of the gap, a dust trap is present where the gas pressure presents a maximum. When the inward migrating dust encounters the maximum, the Epstein gas drag forces the grains to halt their migration and an overdensity appears. In their study, Marzari et al. [1] showed that this overdensity is strong and it appears that a ring of dust is present close to the outer planet. In the inner region, since the dust does not filter through the gap, a hole empty of dust, but not of gas, develops. These two features can be observed in circumstellar disks and maybe a strong piece of evidence for the presence of two giant planets in resonance. In their study, Marzari et al. [1] neglected in the numerical model two potentially relevant effects: the diffusion of dust due to turbulence and the back-reaction of the dust on the gas which may alter the structure of the dust traps.

The introduction chapter of this thesis is devoted to reviewing the fundamentals of protoplanetary disk evolution up to the formation of gaps. Hence, the convergent migration and resonant capture will be discussed and, finally, it will be highlighted the relevance of diffusion and back-reaction on the evolution of the dust.

1.1 YOUNG STELLAR OBJECTS

A disk around a star forms shortly after that part of a molecular cloud from the interstellar medium collapses into a core, giving birth to what is called a "young stellar object" (YSO). Thanks to the heterogeneous composition and velocity field characterized by turbulence, the disk forms due to a non-zero angular momentum. [2]. After its formation, due to the presence of viscosity the disk progressively loses mass due to accretion onto the star. [3]

To distinguish the stages of evolution of a YSO from its formation until right before its culmination into a main sequence star, Lada et al. [4] coined 3 distinct groups, class I, II and III. They are characterized by the following features observed in the spectral energy distribution (SED), respectively: rising emission in the mid-infrared; declining emission, but with a notable excess over the black body stellar photosphere; negligible infrared excess (Figure 1.1). After substantial advancements in the detection of millimeter spectrum, a primordial class 0 was later proposed by Andre et al. which is represented by invisible emission for wavelengths below 10 micrometers. [5] An additional intermediate phase between Class I and II, a refinement of "flat-spectrum sources" (FS), was also proposed by Greene et al. [6]

A young star's life spam therefore begins from Class 0, when it is covered by an optically thick envelope whose mass is still considerably bigger than its core. In this stage a circumstellar system spends only a very small fraction of its total life, around ~ 0.5Myr. [7] Class I represents an early stage consisting of in-falling cloud material and outwards collimated jets of radiation which mark the transition from protostellar to protoplanetary disk. Finally, in class II the protostar appears surrounded by the accretion disk from which is possible to distinguish the black body spectra. The subsequent class III is finally a young star depleted of an apparent disk, but that is still not yet in the main sequence phase.

The slope of the YSO's spectral energy distribution between 2 and 25 μm is the main method used to fit it into a class:

$$\alpha_{IR} = \frac{d \log \nu F_\nu}{d \log \nu} = \frac{d \log \lambda F_\lambda}{d \log \lambda} \tag{1.1}$$

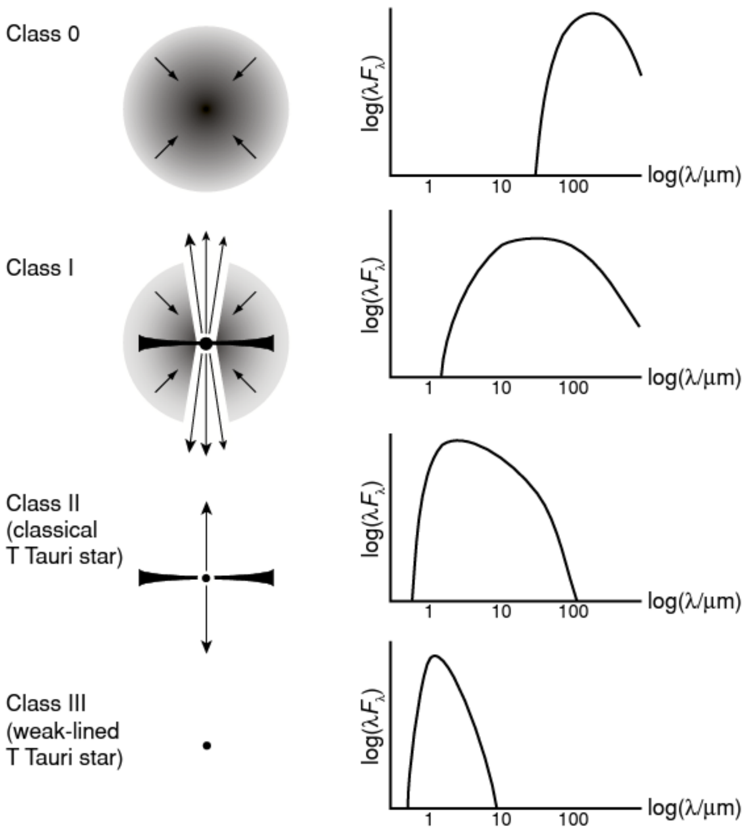

Figure 1.1: Structural and spectral features of the main YSO classifications. [2]

However, the SED classification holds a constraint when it comes to distinguish the amount and distribution of circumstellar material. If the YSO is edge-on to the line of sight, the disk will look more extincted and can be mistaken as being more embedded, lowering its classification. Therefore, physical and observational properties are required in order to properly attribute a YSO to a class, as exposed in Tab. 1.1.

Class	SED slope	Physical properties	Observational characteristics
0	—	$M_{env} > M_{star} > M_{disk}$	No optical or near-infrared emission
I	$\alpha_{IR} > 0.3$	$M_{star} > M_{env} \sim M_{disk}$	Generally optically obscured
FS	$-0.3 < \alpha_{IR} < 0.3$	—	Intermediate between Class I and II
II	$-1.6 < \alpha_{IR} < -0.3$	$M_{disk}/M_{star} \sim 1\%, M_{env} \sim 0$	Accreting disk; strong Hα and UV
III	$\alpha_{IR} < -1.6$	$M_{disk}/M_{star} \ll 1\%, M_{env} \sim 0$	Passive disk; no or very weak accretion

Table 1.1: Table of young stellar object classification extracted from J. P. Williams and L. A. Cieza [3]

This present study is focused on the YSO evolutionary period in which the star belongs to class II, with a mature circumstellar disk in which giant planets have already formed.

1.2 PROTOPLANETARY DISKS

The end of the Class I phase sets the dispersion of the cloud envelope, and consequently also the end of the protostellar formation. The accretion disk here is much less massive than the stellar host. The main physical processes occurring in the subsequent evolution of the disk are now accretion onto the star, photo-evaporation, bulking of larger bodies, and dynamical interactions with stellar or substellar companions. [3]

In order to better understand the disk at this stage and the environment where the planets in formation are embedded, it is important to outline its properties and respective models.

The disk is composed by dust and gas, where the latter represents roughly 99% of the total distribution — much like the rest of the interstellar medium. Dust grains come from the ISM as a mixture of silicates and carbons initially with sizes ranging from 100 Å to ∼0.2 - 0.3 μm, but are subject to growth by coagulation into bigger particles and objects, culminating in the formation of planetesimals and planets. Furthermore, properties such as the gas drag and the radial drift of the dust differ according to the size of the body. On the other hand, dust growth is counterbalanced by other processes that limit its evolution, like the fragmentation and drift of particles; such constraint is still a recurrent problem in the literature when it comes to explain the origin of boulder sized bodies or larger. Birnstel et al., [8] using the model elaborated in a previous work by Birnstel et al., [9] simulated the surface density distribution of the dust populations from a 0.1 $M_\odot$ disk around a solar mass star. The simulation is given by three different time frames (see Fig. 1.2). It is possible to observe that size development quickly ensues, but is halted around a certain threshold called fragmentation barrier, attributed to the collisional fragmentation.

It is possible to measure the total disk mass by relating it directly to the observed flux, F_ν, from the optically thin emission in the submillimeter range:

$$M = \frac{F_\nu d^2}{\kappa_\nu B_\nu(T)} \tag{1.2}$$

where d is the distance to the source, κ_ν is the dust opacity, and $B_\nu(T)$ is the Planck function. The uncertainty due to agglomeration of dust at bodies as big as pebbles or larger, which can hide the emission from enclosed particles, should be accounted for. Therefore, observations at

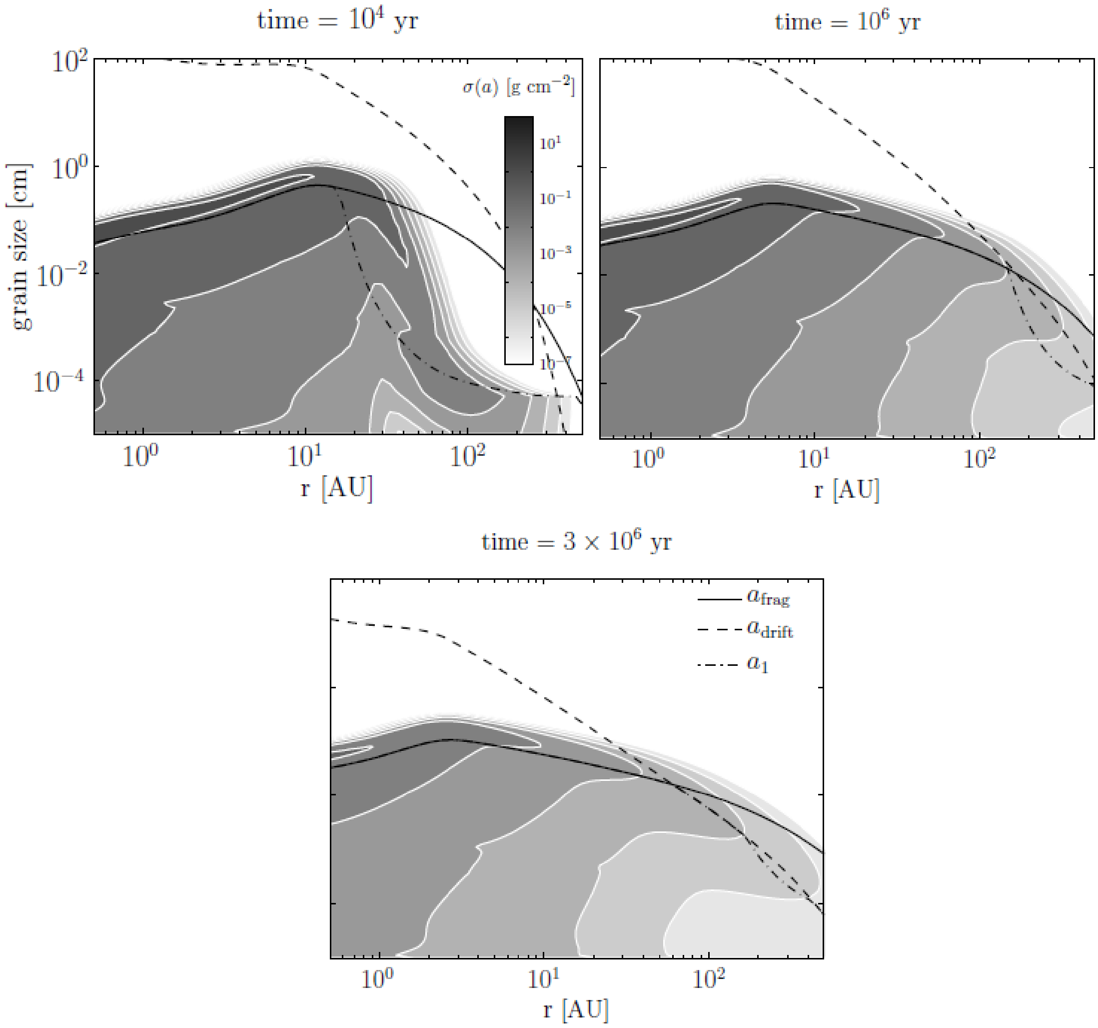
time = 10^4 yr

time = 10^6 yr

time = 3×10^6 yr

Figure 1.2: Surface density distribution of dust, represented in color gradient, according to grain size and disk radius, in three instances of time (10^4, 10^6 and 3×10^6). In this case, turbulence parameter is 10^{-3}. Solid and dashed lines represent, respectively, the dust size limit due to fragmentation and drift, while the dash-dotted line is the largest expected grain size. [8]

a given wavelength λ only constrain the properties of dust up to a maximum grain size $a_{max} \sim 3\lambda$. [3] Andrews & Williams conducted a multiwavelength survey of 153 YSOs in an effort to analyze properties of the dust at outer regions of circumstellar disks and obtained a distribution roughly centered around $5 \times 10^{-3} M_\odot$. [10] Figure 1.3 displays the general radial distribution of surface density inferred by Andrews et al. [11] using their submillimeter survey in the 870 μm thermal emission of nine circumstellar disks in a ~1 Myr-old star-forming region. In the same work, they modeled the surface density evolution and profile as:

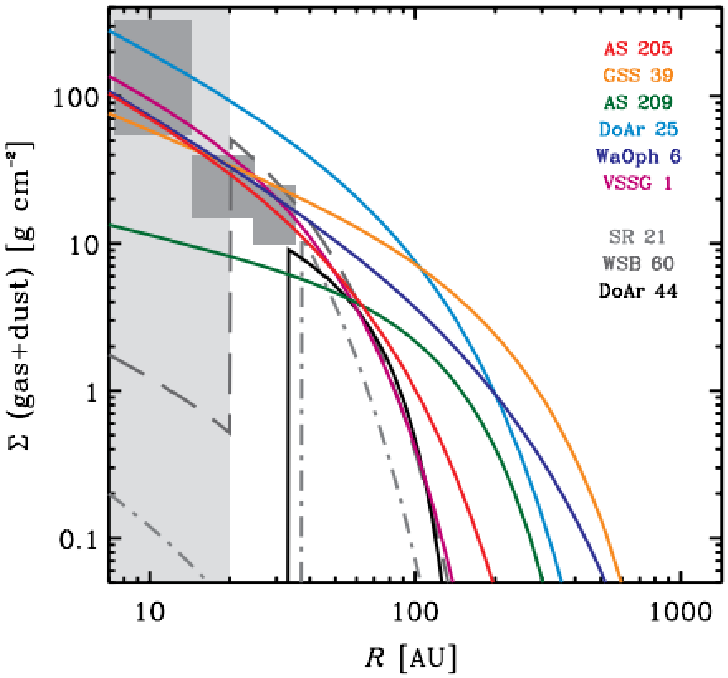

Figure 1.3: Radial surface density profiles (gas+dust). SR 21, WSB 60 and DoAr 44 exhibit central emission cavities. The dark gray boxes represent the region of Saturn, Uranus, and Neptune in the Minimum Mass Solar Nebula. [11]

$$\frac{\partial \Sigma}{\partial t} = \frac{3}{R}\frac{\partial}{\partial R}\left[R^{1/2}\frac{\partial}{\partial R}(R^{1/2}\nu\Sigma)\right] \tag{1.3}$$

$$\Sigma(R) = (2-\gamma)\left(\frac{M_d}{2\pi R_c^2}\right)\left(\frac{R}{R_c}\right)^{-\gamma}\exp\left[-\left(\frac{R}{R_c}\right)^{2-\gamma}\right] \tag{1.4}$$

where M_d is the disk mass, R_c is the characteristic radius from which Σ transforms from power law to exponential density profile (ranging around 14 - 198 AU, according to the same survey), ν is the viscosity and γ specifies the radial dependence of the disk viscosity ($\nu \propto R^{\gamma}$). Andrews et al. agreed on an approximated relation between disk mass and maximum radius given by $M_d \propto R^{1.6\pm0.3}$. [12] Many works on the topic agree that the central density profiles inside R_c have a canonical power law flatter than 1.5, while in the case of Andrew et al. they obtained an average <γ> = 0.9; it is a value that is quite divergent in the literature. The greatest constraint on density measurements is related to the region of the disk closest to the star, where a peak in dust density is located and resolution capabilities are limited.

Hughes et al. [13], using the same density profile from Eq. 1.4, found a rough estimate of the outermost radius, $R_{out} \approx 2R_c$, when investigating four nearby disk systems using the 230 and 345 GHz continuum and the CO's J = 3 - 2 lines from the Submillimeter Array.

The disk mass is not constant throughout the evolution and will be gradually depleted, mainly by accretion of infalling material onto the host star and photoevaporation. The accretion starts as the prevalent method, but then the innermost part of the disk stops being replenished by the outer parts and a gap between the star and the innermost region starts to form and widen. With that, the accretion rate loses its relevance and the star is free to photoevaporate the exposed disk with UV radiation until its final dispersion. Hollenbach et al. [14] give the following estimate for the photoevaporation rate:

$$\dot{M}_{wind} \cong 4 \times 10^{-10} \left(\frac{\Phi}{10^{41}\, s^{-1}} \right)^{1/2} \left(\frac{M_*}{M_\odot} \right)^{1/2} M_\odot\, yr^{-1} \tag{1.5}$$

where Φ is the stellar ionizing flux. The accretion rate in relation to luminosity L, as employed by Takashi et al., [15] is given by :

$$\dot{M}_{acc} = 2 \times 10^{-5} \left(\frac{\eta}{0.1} \right)^{-1} \left(\frac{L}{10^{41}\, erg\, s^{-1}} \right) M_\odot\, yr^{-1} \tag{1.6}$$

with η being the converting efficiency of the rest energy into radiation.

The scale height is a feature of the disks used to model their structural and chemical compositions, fitted according to molecular line observations. Considering that disks are particularly flared (i.e., with increasing vertical dimensions along the radius), it is important to note that the disk evolution also differs according to height. It is expected, for example, that regions of low densities and large scale heights are more sensitive to photoevaporation. Assuming an azimuthally symmetric disk in hydrostatic equilibrium, the density function with dependence in both radius and height is:

$$\rho(R, z) = \frac{\Sigma(R)}{H\sqrt{2\pi}} \exp\left(-\frac{z^2}{2H^2} \right) \tag{1.7}$$

where Σ is given by Eq. 1.4, and z is the vertical height. The scale height, H is depends both on thermal pressure and the vertical stellar gravity and it is also determined by the temperature profile. [3]

As for the temperature profile, Nakamoto & Nakagawa [16] (see Fig. 1.4) modeled the surface and the mid-plane disk temperatures, respectively, as:

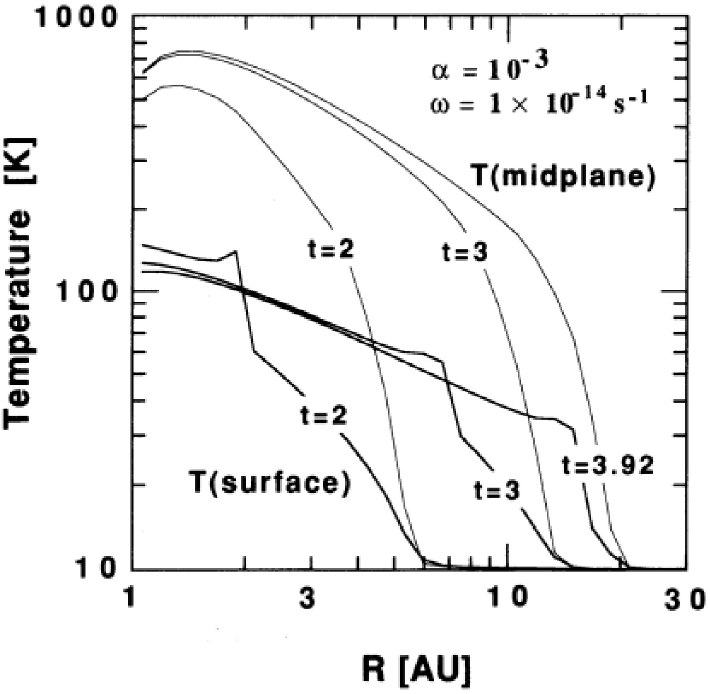

Figure 1.4: Disk temperature radial distribution at the surface (thick lines) and midplane (thin lines), for 3 different ages (2 x 10^5, 3 x 10^5 and 3.92 x 10^5). α and ω are the adopted viscosity parameter and angular velocity of the molecular cloud. [16]

$$\sigma T_s^4 = \frac{1}{2}\left(1+\frac{1}{2\tau_p}\right)(\dot{E}_\nu + \dot{E}_s) + \sigma T_{cloud}^4 \tag{1.8}$$

$$\sigma T_m^4 = \frac{1}{2}\left[\left(\frac{3}{8}+\frac{1}{2\tau_p}\right)\dot{E}_\nu + \left(1+\frac{1}{2\tau_p}\right)\dot{E}_s\right] + \sigma T_{cloud}^4 \tag{1.9}$$

where σ is the Stefan-Boltzmann constant, $\dot{E}_\nu$ is the viscous dissipation rate and $\dot{E}_s$ is the shock-heating rate, τ_p is the disk's mean Planck optical depth. T_{cloud} is the blackbody radiation temperature of the disk surface due to the influence of stellar or interstellar radiation, modeled by Ruden & Pollack [17] as:

$$T_{cloud} = T_* \left[\frac{2}{3\pi}\left(\frac{R_*}{r}\right)^3 + \frac{1}{2}\left(\frac{R_*}{r}\right)^2\left(\frac{H}{r}\right)\left(\frac{d\ln H}{d\ln r}-1\right)\right]^{1/4} \tag{1.10}$$

where R_* is the stellar radius. For a completely optically thin disk, it is assumed an isothermal height distribution, therefore both surface and midplane temperatures are equalized. Otherwise, for the optically thick case, Eqs. 1.8 and 1.9 are related by:

$$T_m^4 = T_s^4 + \left(\frac{3\tau_r}{16\sigma}\right)\dot{E}_\nu \tag{1.11}$$

with τ_r as Rosseland mean optical depth.

As for the velocity profile, unfortunately, there is not a big abundance of surveys due to the difficulty of finding young disks that are bright enough to be observed with spectral lines, usually in the millimeter CO line, but not contaminated by emission from the residual envelope or neighboring cloud. The Keplerian regime produces good fits in the literature, like the one presented by Hersant et al. [18] with velocities given by:

$$u_r = -\frac{3\mu}{2\Sigma r} \tag{1.12}$$

$$u_\theta = \frac{\sqrt{GM_*}}{r^{1/2}} + \frac{r_i^2}{r}(\Omega_* - \Omega_k(r_i)) \tag{1.13}$$

where μ is a surface viscosity coefficient, M_* is the stellar mass, r_i is the inner boundary radius of the disk, Ω_* and Ω_k are the angular velocities for the star and the disk's Keplerian motion. The solution of Ω_k is plotted in Fig. 1.5.

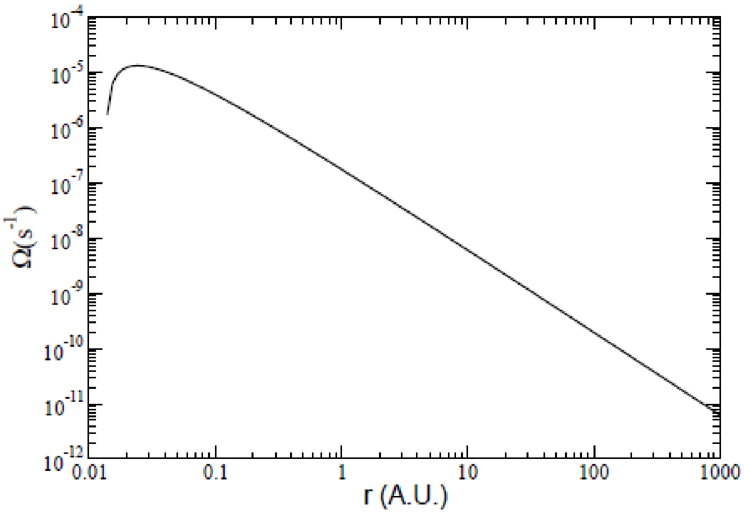

Figure 1.5: Velocity profile in a circumstellar disk in the viscous regime, with Keplerian velocity used in the outer radius. [18]

1.3 TRANSITION DISKS AND GAP FORMATION

Dust may move radially both inwards and outwards due to the gas drag force (the models will be treated in the next section). The final direction is mostly intrinsic to dust particle size and position inside the disk. The net radial velocity, averaged in the vertical direction, is usually inward, provided that the radial gradient of the gas surface density is not too steep. [19] But setting a step apart from theory, observations of the microwave emission at some point started to show that the fall of dust into the protostar is somewhat obstructed by a structure. That is attributed to a narrow local pressure maximum, promoted by the dynamical interactions of the planetary bodies with the outer disk. [20] Said structure, if it manages to efficiently halt the passage and accumulate the dust behind the trapped over-density, will carve a ring-like gap in the disk; a scenario that is also a quite favorable environment for the further growth of particles. [21] This phenomenon marks the beginning of the transition disks.

Even though pressure maxima are normally associated with the presence of massive giant planets, only a minimum planetary mass is required for the planet to impact the system with a visible cavity, and with an ideal low surface density that minimum could be as low as 10 to 20 $M_\oplus$ for orbits at inner and outer radius, respectively. [22] Planets close to that lower limit usually form asymmetric dust gaps. [23]

As an example, Pinilla et al. [21] model the over-density as a simple sinusoidal perturbation on the surface density, given as:

$$\Sigma'(r) = \Sigma(r)\left(1 + Acos\left[2\pi\frac{r}{L(r)}\right]\right) \tag{1.14}$$

where $\Sigma(r)$ is the unperturbed density profile, and $L(r) = fH$ is the perturbing sinusoidal wavelength which is proportional to scale height by a factor f.

To characterize the shape of a transition disk's SED, Cieza et al. [24] elaborated a definition based on the turn-off wavelenght $\lambda_{turn-off}$, which is the point that represents the beginning of the infrared excess over the stellar spectra, and the excess slope α_{excess}. There is no consensual standard in the literature, but one of the most strict transition disk definition, for example, is a $\lambda_{turn-off} > 4.5$ - $8.0\,\mu$m and $\alpha_{excess} > 0$. This definition is translated to the absence of near-infrared excess, steep slopes in the mid-infrared, and large far-infrared excesses, although some other authors may also include some small near-infrared detection. [25] Transition disks are also further attributed to subcategories herein: objects with no detectable near-infrared excess and $\alpha_{excess} > 0$ are called "classical" transition disks; other objects with a sharp rise in their mid-infrared are termed as "cold disks"; disks with a significant flux decrement at all infrared wavelengths, relative to an optically thick disk extended to the dust sublimation temperature, typically have $\alpha_{excess} < 0$ and are referred to as "anemic", "homologously depleted", or "weak excess" disks; disks with evidence of a gap optically thin to starlight separating optically thick inner and outer disk components have been called "pre-transition" disks. See Fig. 1.6 for the characteristic SED diagram of each sub-type. [3]

The occurrence rate of transition disks is expected to be around < 10 - 20%, and the biggest population is of anemic ones. This low rate and the high appearance of late types is often linked to the their short life span.

An observational feature of transition disks is the dip at the SED's infrared excess, which, adopting a rough approach of wavelength being approximately proportional to radius, suggests the location of the solids depletion (see Fig. 1.7). [20] Another signature, for Jupiter-sized planets, is that the filtering process may affect only particles down to a minimum length, therefore

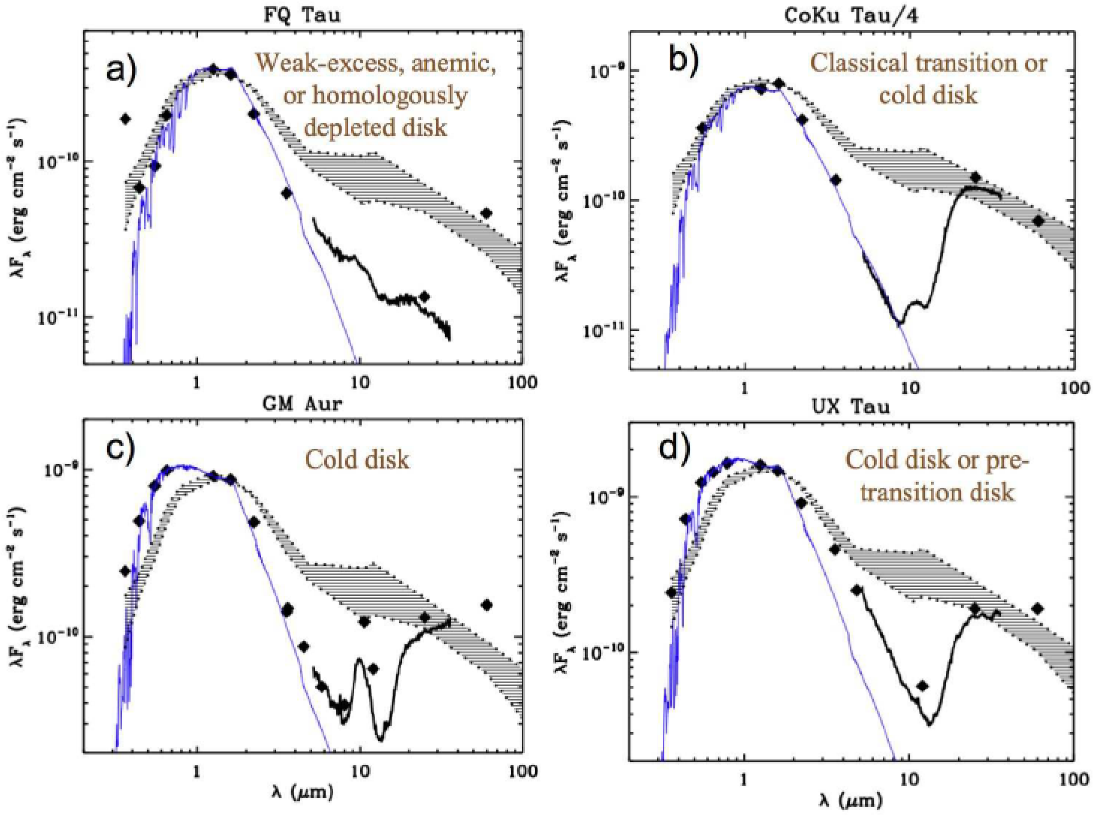

Figure 1.6: SED of transition disk subcathegories. [3]

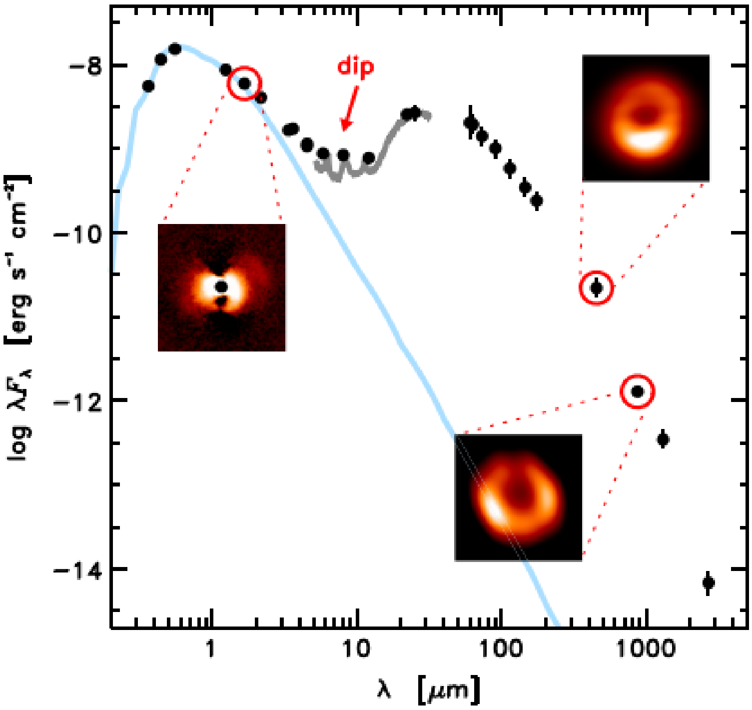

Figure 1.7: SED and relative images of the star SR21 and its disk. The blue line represents the stellar spectra while the gray one is the disk infrared excess that shows dips due to dust depletion. [20]

small ones can penetrate the barrier, creating a different demography of dust size between outer and inner circle. [26]

The model of gap formation relies on the coupling of the gas and dust structures since they are impacted differently in the process. The gaseous gap results from momentum transference between the disk and a massive planet, followed by the detachment of the outer radius from the rest of the disk. The total torque on the planet and minimum necessary to trigger the opening are, respectively:

$$\frac{dJ}{dr} = -\frac{8}{27}\frac{G^2M_p^2a\Sigma_{out}}{\Omega_p^2x_s^3} \tag{1.15}$$

$$\Delta J = 2\pi a x_s\, \Sigma_{out}\, \frac{dl}{dr}\bigg|_a x_s \tag{1.16}$$

with $l = \sqrt{GM_* r}$ as the planetary orbital frequency; M_p and a are the planet's mass and semi-major axis, Σ_{out} is the outer disk's surface density, and x_s is the half-width of the gap. [27]

Therefore, the time frame of the gap formation process is:

$$t_{gap} = \frac{\Delta J}{|dJ/dr|} = \frac{27}{8}\pi \frac{1}{q^2\sqrt{GM_* a}} \frac{x_s^5}{a} \tag{1.17}$$

where q is the planet-to-star mass ratio. [27] In order to allow non-linear dissipation and avoid dynamical instabilities, the thermal condition is evoked, [28] which defines the minimum half-width gap and ratio q as:

$$x_s = 1.16\sqrt{\frac{q}{h}} \geqslant H = ha \tag{1.18}$$

$$q_{th} \cong h^3 = 1.25 \times 10^{-4} \left(\frac{h}{0.05}\right)^3 \tag{1.19}$$

For a different condition in which the disk is a viscous fluid instead, diffusion serves as an opposite process that is responsible for closing gaps. The related closing time frame and the new minimum q ratio for gap opening under this condition are:

$$t_{visc} = \frac{x_s^2}{\nu} \cong 39.8 \left(\frac{\alpha}{0.004}\right)^{-1} P_p \tag{1.20}$$

$$q_{visc} \cong \left(\frac{27}{8}\pi\right)^{1/2} \alpha^{1/2} h^{5/2} \tag{1.21}$$

where P_p is the planet's orbital period, ν is kinematic viscosity, and $\alpha = \nu\Omega/c_s^2$ is the Shakura-Sunyaev parameter. [2]

A generic case which takes into account both the thermal and viscous conditions is described by Lin & Papaloizou [27]:

$$P = \frac{3H}{4r_H} + \frac{50}{qR_e} < 1 \tag{1.22}$$

where r_H is the Hill radius and R_e is the Reynolds number.

In opposition, the dust gap depends on a radial pressure promoted by the planet, and any gas gap can induce a much bigger hole in the dust due to the pressure trapping of solids. Therefore, the minimum planetary mass and opening time frame are much lower in relation to the gas; starting as low as ~0.05 M_J for particles of 150 μm or larger. [29] Furthermore, dust size populations might be affected differently among themselves, with larger gaps attributed to larger grains in decoupled disks. [30]

1.4 Detection methods

Now that the basics of transition disk formation are explained, the next step is to establish an analysis of the dynamics between planets and disks. More specifically, on how pairs of planets behave and how their properties interfere with the structures of the system. The first step is to examine the best methods to detect planets that are able to measure important indicators of their motion patterns.

As of September 2022, more than 5100 exoplanets have been confirmed, spread over 3800 planetary systems, with the considerably largest number of observations done by radial velocity and transit techniques, which are indirect methods. [31] The reason for the choice of indirect approach is due to the fact that planets are faint objects and are difficult to resolve from the light of the host star, which makes direct detection unreliable and biased towards massive and young, brown dwarfs at far away orbits. [32]

The well-known radial velocity method relies on the wobble of the star caused by its gravitation interaction with the system around the common barycenter. The range of this motion is relatively small compared to the resolvable distances. So instead, as being an indirect method, high-precision spectrography is taken in order to measure the radial velocity in terms of inclination angle and its associated cyclical amplitude. They are obtainable from the Doppler effect acting on the spectra of the star along the line of sight. When searching for a single planet, it is possible to use a Keplerian model analytically, but when it comes to multi-planetary systems, planet-planet interactions can significantly alter the radial velocity signature. Therefore, a full dynamical (Newtonian) fit involving an N-body code can be used to ensure the short and long-term stability of the solution. A reasonable initial guess for the orbital parameters is necessary to reach a good fit for the numerical solution, which otherwise may also lead to extensive computational time. [33] The main obtainable parameters from this method are the planetary mass (in terms of $\sin i$), period, semi-major axis, eccentricity, and argument of the pericenter. Unfortunately, the method is biased towards massive planets at far away orbits, since these properties highly influence the wobble amplitude. It is also important to note that, when the inclination of orbit is unknown, a bigger uncertainty is applied to the amplitude and planet mass.

The transit method holds the largest number of discoveries to date and takes advantage of the passage of planets right in front of the line of sight of the host star. The eclipsing object is measured by a dip of flux in the photometric surveys. The main obtainable parameters are: planetary radius, period, semimajor axis, impact parameter, and inclination. When allied with a follow-up mission of spectrographic surveys, not only it enables the confirmation of the planet detection, but also confirms the planetary density by combining the measured mass and radius, allowing to characterize the body. For a multi-planet system, in the best-case scenario in which more than one planet is transiting in front of the same star, a series of dips of different frequencies can be observed. Considering that gravitational interactions are possible, neighboring invisible planets can perturb the orbit of the observed transit, causing irregularities in the orbital period. If the transit times are compared to a fit, the so-called transit time variation can be confirmed, even if the perturbing planet is not in line of sight. The method is limited mostly to signal-to-noise dependence and the low probability of observing an eclipsing planet. It is biased towards massive and short-orbit bodies (hot Jupiters) around small stars.

Here, it is also worth mentioning the microlensing technique. It uses the gravitational curvature of the light from a background source, caused by the passage of a target host star. The method can also be a tool to confirm a system with planets in free-floating motion or distant orbits but lacks viability due to its scarcity of occurrence. [34]

1.5 MEAN MOTION RESONANCE

Once the mean motion and other orbital parameters of the detected exoplanets are obtained, it is possible to infer the resonance between pairs. Such relation is given as:

$$n_2(p+q) - pn_1 \cong 0 \tag{1.23}$$

where n_1 and n_2 are the mean motion of the respective bodies in the pair, while p and q are positive integers. The ratio between n_1 and n_2 is thus given by $(p+q)/p$, which is referred to as the mean motion resonance (MMR). [32] The ratios tend to float around integers, like 2:1 and 3:2.

Another way of defining MMR is by the formula of resonance angle:

$$\theta_i = (p+1)\lambda_1 - (p)\lambda_2 - \varpi_i \tag{1.24}$$

where λ is the mean longitude and ϖ is the longitude of pericenter, while index $i = 1, 2$ refers to the given parameter for the inner and outer planet, respectively. Note that here, $q = 1$. The dependence on the longitude of pericenter that accounts for the precession of the orbit is what makes the resonance angle a good definition of MMR capture. An angle that is circularized in a range of 0 to 2π indicates the absence of resonance, while an angle that oscillates around a given value represents resonance around the represented commensurability. Large oscillations may cause the MMR to dissolve.

One last possibility of defining resonance is by the relation: $(p+q)n_2pn_1qg_i = 0$, where g_i is the eigenvalue of ϖ_i. [35]

It is important to note that with an eventual migration process (as will be discussed in the next subsection), planets will tend to approach each other. That is translated to an increase in periods and a lowering of the period ratio caused by perturbations. The final result is the overthrowing of the separation between close resonances. This is phenomenon is called resonance overlap and is a source of chaotic motion, often leading to capture break. [36] The overlap depends on the planet-to-star ratio:

$$\varepsilon_p = \frac{m_1 + m_2}{M_*} \tag{1.25}$$

and will take place if, in the case of a first-order MMR, the semi-major axis ratio is: [37]

$$\frac{a_2 - a_1}{a_1} \lesssim 1.46(\varepsilon_p)^{2/7} \tag{1.26}$$

1.6 Convergent migration and resonance capture

It is important to note that said resonance is not an auto-sufficient process and depends mainly on the simultaneous convergent displacement of the pair. It causes one planet to approach the other and lock it in an orbital period ratio, even though it is not always a guaranteed result. K. Batygin [38] investigated the criteria for certain capture, taking in account the unrestricted elliptic three-body problem, and stipulated the formula:

$$\left[\frac{3\,\xi M_*\,(2(k-1)^2\,m_2 + k^2 m_1 \xi)}{\left(\left(f_{res}^{(1)}\right)^2 m_2 + \xi\left(f_{res}^{(2)}\right)^2 m_1\right)^2}\right]^{2/3} \times \left(\left(f_{res}^{(1)}\right)^2 e_1^2 + \left(f_{res}^{(2)}\right)^2 e_2^2 + 2 f_{res}^{(1)} f_{res}^{(2)}\, e_1\, e_2\, cos(\Delta\varpi)\right) \leqslant 6 \tag{1.27}$$

where k is an integer greater than unity, f_{res} is a function of order unity that slightly depends on the semi-major axis ratio (a_1/a_2), and $\xi = ((k-1)/k)^{1/3}$. For cases in which this condition is not met, figure 1.8 exemplifies the probabilistic profile for the specific case of a 3:2 resonance.

More specifically, D'Angelo & Marzari [39] defined the condition for the 1:2 resonance cap-

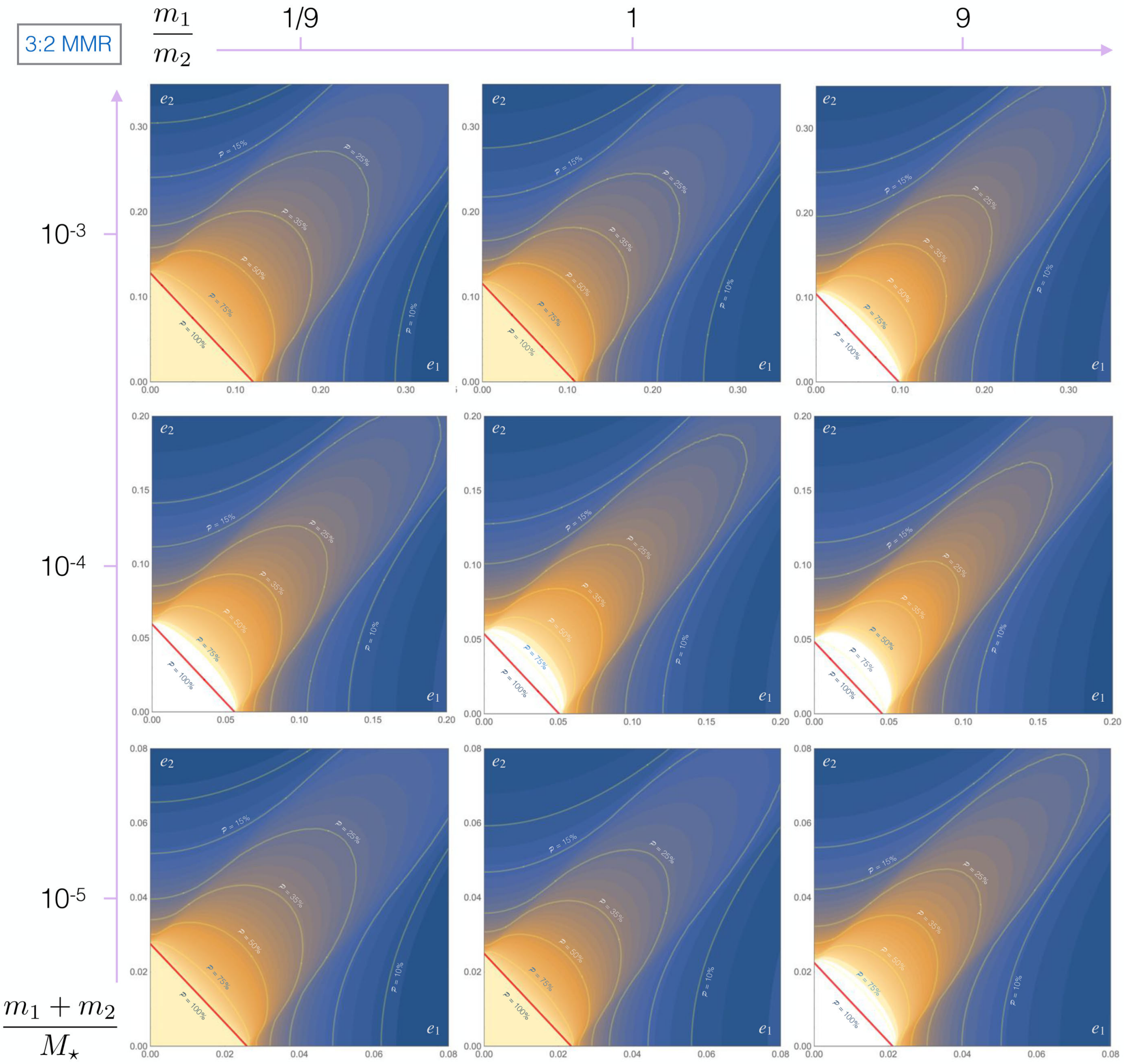

Figure 1.8: Capture probability distribution for the 3:2 resonance. Plots are distributed along $(m_1 + m_1)/M_*$ and m_1/m_2 in the vertical and horizontal axis, respectively. Inside each plot, represented by e_1 x e_2, the brightest orange zone inside the triangle represents the 100% capture, while probability decreases towards the dark blue. [38]

ture in a type I migration as:

$$\left(\frac{a^2\Sigma}{M_*}\right) \lesssim \left(\frac{H}{a}\right)^2 \left(\frac{M_*}{M_2}\right) \left(\frac{M_1}{M_*}\right)^{4/3} \tag{1.28}$$

with M_1 and M_2 being the mass of the inner and outer planet, respectively, and a the radial distance.

The convergent migration phenomenon in a planetary system formation is attributed to different processes. Among them, it is possible to cite: tidal dissipation, outward migration of embryos, and disk-planet interaction.

Tidal dissipation can be exemplified by the evolution of Io. According to one of the models, due to tidal interaction with Jupiter, Io spiraled outwards and got caught in a 2:1 resonance with Europa. As a consequence, another resonance of Europa with Ganymede was then established. [40]

Rapid outward migration of embryos is caused by the gravitational scattering of the planetesimals along with the effects of aerodynamic gas drag. This is particularly mentioned as one of the most successful phases of embryo growth. [41]

Disk-planet interaction is the most notable migration mechanism. The gravity potential of a planet promotes the propagation of density waves on a disk through Lindblad and corotation resonances. As a reaction, a torque from each excited wave acts back on the planet. The final torque is the difference between the positive (inwards the orbit) and negative (outwards) Lindblad resonances and dictates the direction of migration. This development is cataloged into types I, II, and III. [42]

Type I migration takes place when the planet does not have enough mass to impact the disk and carve a gap in it. For an inward transport, it is a matter of about 0.1 – 1 Myr until the planet is lost into the star. This gives rise to the Type I problem, since it contradicts the regular time frame of planetary growth (around 1 to 10 Myr), implying that it should not be possible to observe surviving type I migrating planets.

However, the scenario changes for planets that reach a mass greater than ~30 – 100 $M_\oplus$ before being accreted. If the angular momentum is successfully transferred to the disk and is not carried away by the spiral waves, the material inside or outside the orbit can respectively lose or gain angular momentum, clearing a patch in the disk. Because the density in the co-orbital region is reduced, co-rotation torques are no longer of importance for larger planet masses. Lindblad torques are also reduced, resulting in slowing down the planet migration in relation to type I. The planet becomes coupled to the viscous evolution of the disk, while having its migration rate significantly decreased, thus marking the beginning of type II. The required mass varies due to disk parameters like viscosity and scale height. [43]

Furthermore, planets in a type I regime, when co-rotating resonance is strong enough, can have their migration slowed down and even reverted. This leads to type III, or runaway migration, which is not truly resonant, but depends strongly on the gas flow in the planet vicinity and does not have a predetermined direction, but tends to go inwards thanks to the Lindblad torque. [44]

Planetary population synthesis and N-body simulations are the most used approaches to study the migration evolution.

Population synthesis adopts Monte-Carlo techniques to sample planetary populations to be compared with observed ones. The objective is to try to achieve the properties (orbital elements and masses, especially) that produce the best fit with the observational data.

N-body simulations take into account the gravitational interaction of the particles in the system and trace their Keplerian dynamical evolution in order to predict planet growth and migration; it is a technique that has the advantage of including important planet-planet interactions that can induce orbital changes, as opposed to the single-planet approach adopted by most of population synthesis studies. [44]

The condition for resonance capture pends mostly on the time they take to establish this interaction which must be longer than the libration time, while the mean motion ratio depends on the masses, the relative migration speed, and the initial separation of the planets. Ogihara & Kobayashi [45] investigated empirically the critical migration timescale for closely spaced first-order resonances (pair of mean motions with a difference of one unit, e.g., 2:1, 3:2 and 4:3), and obtained the following formula:

$$f_{a,crit} \approx C \left(\frac{M_1}{M_\oplus}\right)^{-4/3} \left(\frac{M_*}{M_\odot}\right)^{4/3} T_K \tag{1.29}$$

where constant C depends on the mass and commensurability ratio of the pair and T_K indicates the orbital period of the inner body.

The capture promotes the increase of eccentricity, which can be counteracted by damping factors like the outer and inner disks. The 2:1 is taken as first-order resonance ($q = 1$), usually a result of two distant planets in convergent migration, and is common for planets provided that migration is not too fast. Important to note that divergent migrations, i.e., a pair that changes semi-major axis while separating from each other, do not promote resonance capture.

1.7 Outward migration

If the resulting torque of in-falling planets is reverted positively due to the local reduction of the surface density, the migration changes its radial direction and begins to move away from the star. For that, the planets need to be massive enough to affect the surface density of the disk and close enough to each other so that their density gaps overlap (figure 1.9). This is usually the case for pairs with a semi-major axis separation of at most several times the sum of the planets' Hill radii. [39] The shape and depth of the common gap strongly depend on the type of resonance ratio and on the disk parameters.

A great example of simultaneous outward migration is described by the Grand Tack hypothesis, in which Jupiter and Saturn, during their formation era, moved towards the Sun until they reached ∼1.5 and ∼2.0 AU, respectively. As consequence, they got trapped in a 3:2 mean motion resonance together, then reversed the direction of motion, facing outwards. The 3:2 ratio was preserved until the final dissipation of the disk. [46]

Marzari et al. [1] carried out two-dimensional, hydrodynamical simulations of a disk populated by a pair of resonant giant planets in outward migration in order to analyze the evolution of dust particles in such a scenario and observed some important properties. First, the dust component in the transition disk expands over a larger distance if compared to the gas; the latter maintains its shape and moves along with the planets, which in the long term culminates in dissociating one component from the other. This decoupling generates a mark on the dust gap that indicates the beginning of the outward migration and therefore the moment of resonance capture. Second, the pair of planets in this condition would create the over-density of dust in the inner edge of the outer gas ring already mentioned before. This feature is more prominent in the 2:1 commensurability over the 3:2. The 2:1 is responsible for a very effective blockade of dust evidenced by the observable bright ring in high-resolution images. The 3:2 allows smaller dust particles to cross the edge and reach the planets, filtering the ones larger than 1 cm creating a complex distribution of sizes.

But as mentioned by the authors, two factors were not accounted for in the execution of the simulation.

The diffusion may reduce the local density of the solids found at the exterior of Saturn's orbit. It is possibly caused by a difference in relative speed between the two materials. The result is the turbulence transport along the gap edges and consequently the drift of dust. Diffusion may provide different structural changes to the disk. Take for example the case explored by Zhu et al. [47] in their two-dimensional HD simulations. The dust trapping, when under the influence

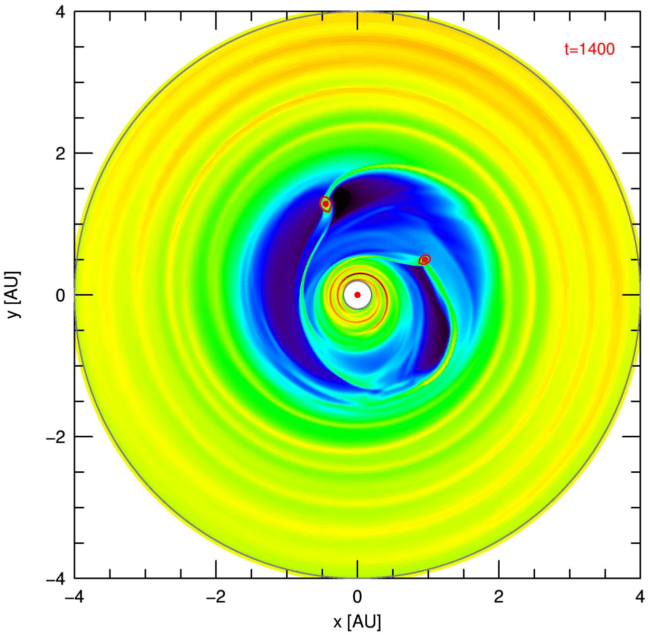

Figure 1.9: Density profile of circumstellar disk that possesses a pair of planets in 2:1 resonance sharing the same gap. [44]

of turbulence, allows particles smaller than 0.1 mm to jump the barrier. This selective filter has a dependence on stellar accretion rate, viscosity parameter and planet mass. By analogy, it is also possible to cite the work of Schobert & Peeters [48]. From their numerical implementation, they registered a vertical elevation of the disk, starting from the innermost tip. This change reflected in the cooling of the rest of the disk, thanks to a higher protection from the stellar radiation. Also, an increase of dust-to-gas ratio was registered due to lower temperatures, ideal for dust growth.

The back-reaction of the dust particles onto the gas. It becomes relevant as soon as the dust-to-gas ratio becomes accentuated (~ 1) and the deformation timescale overthrows the restoration one. Back-reaction may alter the morphology of the outer gap edge by the resulting outward flow of gas from a pressure gradient, causing the redistribution and flattening of the bump [49] and allowing the passage of particles through the filter. [50]

Therefore, further study with simulations that contemplate these missing attributes is imperative to clear all the suspicions.

2
Models

In order to carry out the proposed investigation, an adapted version of the algorithm created initially by Masset [51] and improved by Llambay & Masset [52] was adopted. It is called FARGO3D and is available on the homonym website [53]. It is offered as a versatile multifluid hydrodynamical/magnetohydrodynamical (HD/MHD) code on an Eulerian mesh that runs on clusters of CPU's or GPU's, with special emphasis on protoplanetary disks on Cartesian, cylindrical or spherical geometry. Furthermore, this study made use of the enhanced numerical method based on FARGO3D, presented by Llambay et al., [54] which employs different species of fluids and dust size populations. In this section, the main code, the multi-fluid implementation, and the two simulation setups will be explained; the first being the one employed by Marzari et al. [1] and the second being my own addition of diffusion and back-reaction.

2.1 FARGO3D

In regards to the base FARGO3D code [52], its main operations revolve around the Euler's equations of fluids. Among them is the continuity equation, which is given as:

$$\frac{\partial \rho}{\partial t} + \nabla \cdot (\rho v) = 0 \tag{2.1}$$

where ρ is the volumetric density and v is the fluid velocity in relation to the mesh. Next, Navier-Stokes equation is written as:

$$\rho\left(\frac{\partial v}{\partial t}+v\cdot\nabla v\right)=-\nabla P+\frac{1}{\mu_0}(\nabla\times B)\times B+\nabla\cdot T+F_{ext} \\ -\left[2\Omega\times v+\Omega\times(\Omega\times r)+\dot{\Omega}\times r\right]\rho \quad (2.2)$$

where P is the pressure due to superficial forces, B the magnetic field (applied only in MHD simulations), F_{ext} is any external force; the last term of the equation compensates for possible rotations of the mesh in the vertical axis. T is the stress tensor, which can be recognized as:

$$T=\rho\nu\left[\nabla\nu+(\nabla\nu)^T-\frac{2}{3}(\nabla\cdot\nu)\,I\right] \quad (2.3)$$

where ν is the kinematic viscosity and I is the unit tensor of the same rank as the tensor $\nabla\nu$.

The conservation of volumetric energy, in a non-conservative form, is:

$$\frac{\partial e}{\partial t}+\nabla\cdot(ev)=-P\,\nabla\cdot v \quad (2.4)$$

Furthermore, these equations are tied together with the equations of state:

$$P=c_s^2\rho \quad (2.5)$$

$$P=(\gamma-1)e \quad (2.6)$$

where c_s is the isothermal sound speed and γ is the ratio of specific heats at constant pressure and volume. Eq. 2.5 is calculated when Eq. 2.4 does not need to be solved, otherwise Eq. 2.6 is employed.

The code subdivides the fluid into cells. Scalar quantities (internal energy and density) are related to the enclosed content inside each one of them, while vectorial quantities (velocity and magnetic field) are connected to the surface of the cell limits. A mesh of cells that decomposes a fluid under this configuration is denominated as *staggered* (see Fig. 2.1). Cells are spatially distributed according to their index, i, j, and k, each one related to a different direction. The indexes are written by the respective quantities as a subscript. Therefore, scalars, which are cell-centered, will be given integer indexes (e.g., i, j, k), while vectorial ones, measured at the faces between cells, are given half-integers (e.g., $i+1/2, j+1/2, k+1/2$).

FARGO3D solves the hydrodynamic equations step-by-step using operator splitting and upwind techniques, as introduced by the precursor ZEUS-2D. [55] The complete cycle, denominated as a "full update", is described by Fig. 2.2, which enlists steps from 1 to 12. Steps 7 (source) and 12 (transport) are responsible for the calculations of the hydrodynamics equa-

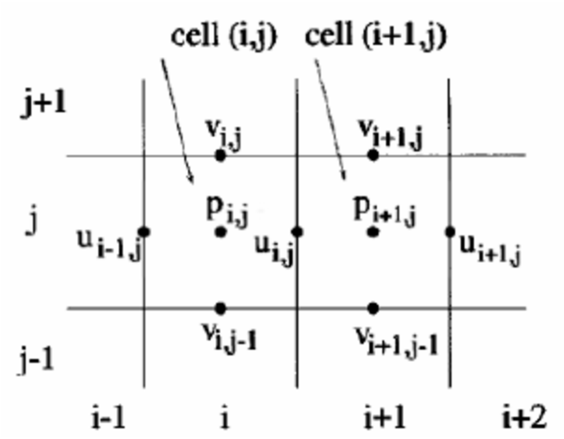

Figure 2.1: Simple example of a staggered mesh, with scalar and vectorial quantities respectively in the center and on the surface of each cell with their respective subscripts. [56]

tions. Since the project does not implement any magnetic field in the calculations, the related steps located inside blue-colored boxes (8, 10, 11) will not be specified here.

To describe the operator splitting technique, consider a function $A(U)$ which can be separated into $A = A_1 + A_2$. Given an equation in the form $\partial_t U + A(U) = 0$, its solution can be written as a linear combination of:

$$\begin{aligned} \partial_t U_1 + A_1(U_1) &= 0 \qquad & \frac{U_1 - U_0}{\Delta t} &= -A_1(U_0) \\ \partial_t U_2 + A_2(U_2) &= 0 \qquad & \frac{U_2 - U_1}{\Delta t} &= -A_2(U_1) \end{aligned} \tag{2.7}$$

where the left column is written in differential form and the right column is in finite form.

It is possible to simplify the HD equations in a general way, decomposing them into three terms: a partial time derivative of a quantity Q, plus the divergence of the same quantity times velocity, resulting in the source term S:

$$\partial_t Q + \nabla \cdot (Qv) = S(Q, v, t) \tag{2.8}$$

It is possible to connect Equation 2.8 to the function $A(U)$, such that $A_1 = -S$ and $A_2 = \nabla \cdot (Qv)$. Substituting them in Eq. 2.7:

$$\partial_t Q = S(Q, v, t) \tag{2.9}$$

$$\partial_t Q + \nabla \cdot (Qv) = 0 \tag{2.10}$$

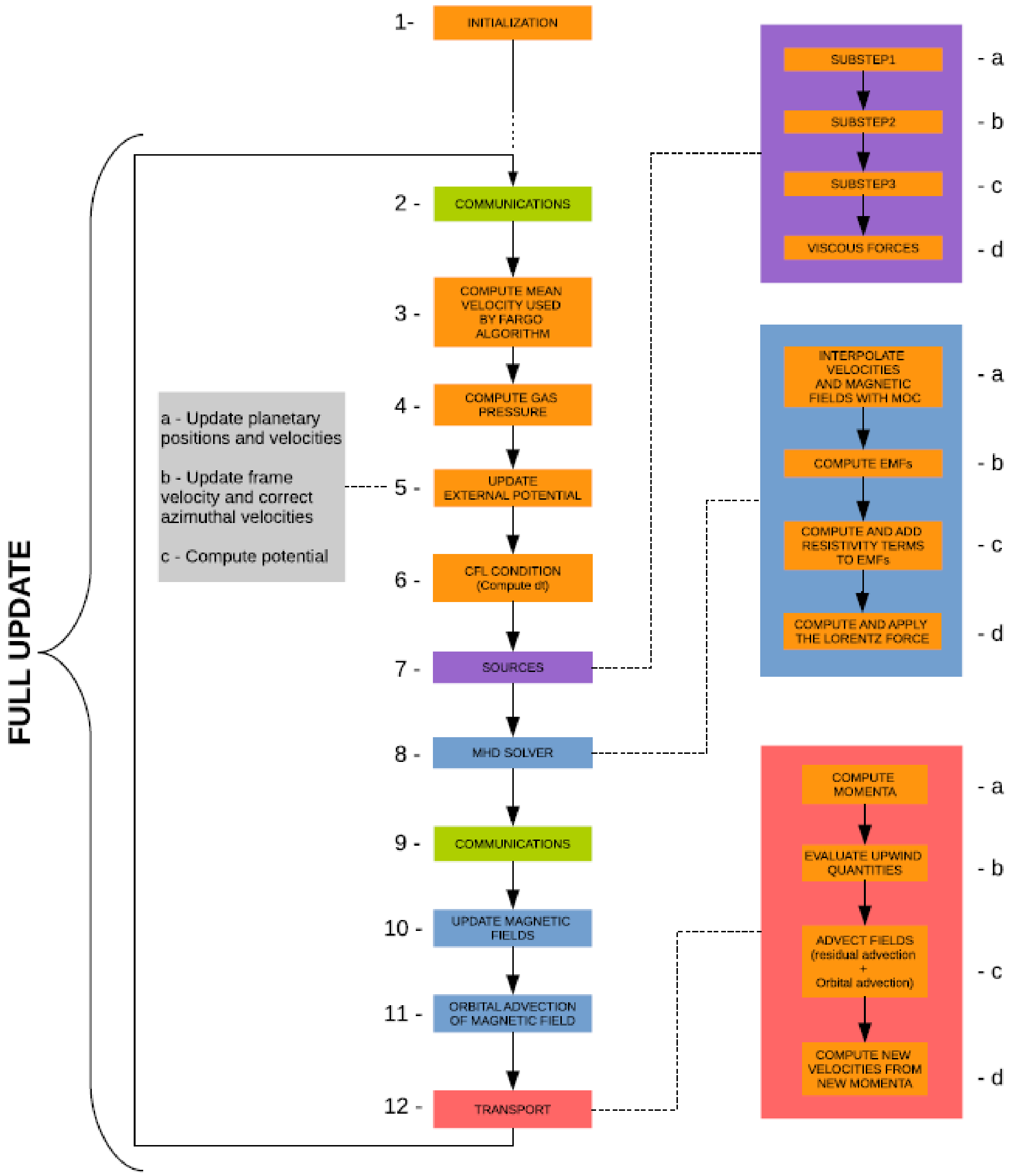

Figure 2.2: Flowchart describing a full cycle of operations, called a full update, which is divided into different substeps. [52]

which splits the problem into two parts, the source and transport steps, respectively; hence the operator splitting. Therefore, the technique consists of applying Equation 2.9 to obtain $Q(t_0) \rightarrow Q_1$, followed by Equation 2.10 that handles $Q_1 \rightarrow Q_2 = Q(t_0 + \Delta t)$.

Applying the HD equations to spherical coordinates, it is possible to distinguish which terms are dealt with in which step. Starting with the continuity equation (Eq. 2.1), the divergence of velocity vector is:

$$\nabla \cdot u = \frac{1}{r^2}\partial_r(r^2 u_r) + \frac{1}{r\sin\theta}\partial_\varphi u_\varphi + \frac{1}{r\sin\theta}\partial_\theta(u_\theta \sin\theta) \tag{2.11}$$

Navier-Stokes (Equation 2.2), adopting the material derivative D_t, in the r, φ, θ direction becomes:

$$D_t v_r = \frac{v_\theta^2 + (v_\varphi^t)^2}{r} - \frac{\partial_r P}{\rho} - \partial_r \Phi \tag{2.12}$$

$$D_t v_\varphi = -r\sin\theta\dot{\Omega}_f - \frac{v_\varphi v_r + v_\varphi v_\theta \cot\theta}{r} - 2\Omega_f(v_r \sin\theta + v_\theta\cos\theta) - \frac{\partial_\varphi P}{r\sin\theta\rho} - \frac{\partial_\varphi \Phi}{r\sin\theta} \tag{2.13}$$

$$D_t v_\theta = -\frac{v_\theta v_r}{r} + \frac{(v_\varphi^t)^2}{r}\cot\theta - \frac{\partial_\theta P}{r\rho} - \frac{\partial_\theta \Phi}{r} \tag{2.14}$$

where $v_\varphi^t = v_\varphi + r\sin\theta\Omega_f$ is the azimuthal velocity in the inertial frame. Taking the continuity equation and applying to Equations 2.12 to 2.14:

$$\partial_t(\rho v_r) + \nabla\cdot(\rho v_r v) = \rho\frac{v_\theta^2 + (v_\varphi^t)^2}{r} - \partial_r P - \rho\partial_r\Phi \tag{2.15}$$

$$\partial_t(\rho j) + \nabla\cdot(\rho j v) = \rho D_t j = -\partial_\varphi P - \rho\partial_\varphi\Phi \tag{2.16}$$

$$\partial_t(\rho r v_\theta) + \nabla\cdot(\rho r v_\theta v) = \rho(v_\varphi^t)^2\cot\theta + \partial_\theta P + \rho\partial_\theta\Phi \tag{2.17}$$

where $j = r\sin\theta v_\varphi + r^2 sin^2\theta\Omega_f$ is the specific angular momentum.

Therefore, in the place of quantity Q (Equations 2.9, 2.10), the transport step will take in $\rho, \rho v_r, \rho j, \rho r v_\theta$ and e, as expressed in the right-hand side of Equations 2.13 in the first to third terms, and in Equation 2.14 in the first term. The right-hand side of Equations 2.15 to 2.17 (exposed above by a factor ρ) will then be dealt with in the source step. In order to translate it to coordinate systems other than the spherical one, it is necessary to transport different quantities, as expressed in Table 2.1.

Geometry	X-direction	Y-direction	Z-direction
Cartesian	ρv_x	ρv_y	ρv_z
Shearing sheet	$\rho(v_x + 2\Omega_f y)$	ρv_y	ρv_z
Cylindrical	$\rho(r v_\varphi + r^2 \Omega_f)$	ρv_r	ρv_z
Spherical	$\rho(r v_\varphi \sin\theta + r^2 \sin^2\theta \Omega_f)$	ρv_r	$\rho r v_\theta$

Table 2.1: Quantities to be transported in the three dimensions according to the adopted geometry. [52]

In the source step, the represented elements in play are the centrifugal force, the pressure gradient, the body forces, and the work from pressure forces. This stage is further divided into three distinct substeps, as initially proposed by Stone & Norman [55], represented in Figure 2.2 at the purple box from a to c: substep 1 is responsible for updating the velocities by pressure gradients, gravitational forces, and inertial forces, by operating the right-hand side of Equations 2.15 to 2.17; substep 2, based on the partially updated velocities, implements an artificial viscosity stress and the related dissipation (as done by Tassoul [57], for example); substep 3 employs the work done by pressure forces, in case the energy equation (Eq. 2.4) is calculated. The operations are applied to the velocity vector (more precisely to $\partial_t v$, as in Equation 2.9). Between the transition of substeps, an average among cells in the mesh is calculated.

In contrast, the transport step reproduces the conservation law with respect to fluxes, as described by Equation 2.10. It can be written, using the divergent theorem in a finite difference, as:

$$[Q^{n+a}_{i,j,k} - Q^{n}_{i,j,k}]V = -\Delta t[F^{x}_{i+1/2,j,k} - F^{x}_{i-1/2,j,k}]^{n+1/2} \tag{2.18}$$

$$[Q^{n+b}_{i,j,k} - Q^{n+a}_{i,j,k}]V = -\Delta t[F^{y}_{i,j+1/2,k} - F^{y}_{i,j-1/2,k}]^{n+1/2} \tag{2.19}$$

$$[Q^{n+1}_{i,j,k} - Q^{n+b}_{i,j,k}]V = -\Delta t[F^{z}_{i,j,k+1/2} - F^{z}_{i,j,k-1/2}]^{n+1/2} \tag{2.20}$$

where V is the volume of the cell. F is the flux in the x, y, z directions, respectively. The subscripts of Q and $F(i, j, k)$ are related to the cell position in the mesh, and half subscripts, such as the ones from F, represent the surface limits between cells. Q's superscripts represent the intermediate stages, which depend on the order of calculation. In the particular sequence demonstrated above, Equation 2.18 calculates the difference between the initial value of Q (step n) and the resulting Q pertaining to the computation of flux in the x-direction (partial step $n + a$). Then, it is followed by Equations 2.19 and 2.20 with computations respectively in the y and

z directions, advancing to partial step $n + b$ and finishing with the next full step $n + 1$. This process is equivalent to calculating the second and third terms of Equation 2.13 and the first term of Eq. 2.14, at the right-hand side of both formulas, and is depicted in Figure 2.2 as the letter c by the red box of the transport step.

The correction of changes in the rotation frame takes place out of the transport step, in substep 5b (Figure 2.2), by applying the following term to the initial azimuthal velocity of the cell's surface:

$$v'_{\varphi,ijk} = v_{\varphi,ijk} - (\Omega'_f - \Omega_f) r \sin\theta \tag{2.21}$$

where Ω_f and $v_{\varphi,ijk}$ are the initial values for frame rotation rate and azimuthal velocity, respectively, while Ω'_f and $v'_{\varphi,ijk}$ are the final ones.

The upwind evaluation of a flux F at half-time step on the face center of a cell (step 12b, Figure 2.2) is expressed as:

$$F^{n+1/2}_{x,i+1/2} = v^{n}_{x,i+1/2}\, Q^{*}_{x,i+1/2}\, S_{i+1/2} \tag{2.22}$$

where v is the velocity before the beginning of the step at the cell surface and half step; Q^* is an interpolated value of a generic quantity Q (density, energy, momentum), also at cell surface, acquired from a zone-wise linear reconstruction of van Leer's slopes [58]. Calculations are executed only in one dimension (in the x-direction, for the case above).

In the transport step, the products of quantities are handled. Together, they are dimensionally related to momentum but are not located at the same point of a cell. Therefore, the cell-centered left and right momenta are introduced, respectively:

$$\Pi^-_i = \rho_i v_{i-1/2} \tag{2.23}$$

$$\Pi^+_i = \rho_i v_{i+1/2} \tag{2.24}$$

where left momentum assumes the velocity from the left face of a cell ($v_{i-1/2}$), while the right momentum the one at the right surface ($v_{i+1/2}$); both with cell-centered density ρ_i. They are calculated at the initial substep 12a (Fig. 2.2), then the final velocity is computed at the end of the transport step, substep 12d, by taking in the new momenta and densities:

$$v^{n+1}_{i-1/2} = \frac{\Pi^{+,\,n+1}_{i-1} + \Pi^{-,\,n+1}_{i}}{\rho^{n+1}_{i-1} + \rho^{n+1}_{i}} \tag{2.25}$$

where indexes i and $i-1$ represent, respectively, a given cell and its predecessor in the mesh. Equations 2.23 to 2.25 refer to the Cartesian coordinates, but they can be converted to different geometries by changing the transported quantities as in Table 2.1.

The momenta in a full cycle are conserved by including the pressure between the cell's superficial limits in the fluxes. Although, this process is handled in the substep 7a instead (Fig. 2.2) in order to keep up with the impact of the source term. Such conservation with machine accuracy is attributed to the satisfied shock jump conditions in isothermal setups in the code, regardless of artificial viscosity and vortensity. [52]

To guarantee the stability of the full cycle, it is important to maintain its extent within a limited time frame for the sake of containing the properties of a cell inside itself in each step; this is named CFL or Courant condition and is dealt with in step 6 (Fig. 2.2). From Stone & Norman [55], the time maximum is:

$$\Delta t = C \cdot min \left[\left(\sum_i \Delta t_i^{-2} \right)^{-1/2} \right] \tag{2.26}$$

where C is called Courant number, and is fixed in the code at $C = 0.44$ by standard. Δt_i is dependent on the individual processes, as listed below:

- Sound waves: $\Delta t_1 = \Delta j / C_s$, where C_s is the speed of sound.
- Fluid motion: $\Delta t_2 = \Delta j / |V_j|$.
- Artificial viscosity: $\Delta t_3 = C_2 |\Delta j / \Delta v_j|$, where $C_2 = 4\sqrt{2}$ is a constant, and $\Delta v_j = v_{j,\, i+1/2} - v_{j,\, i-1/2}$ is the difference between successive values of v_j.
- Viscosity: $\Delta t_4 = \Delta j^2 / (4\nu)$, where ν is the kinematic viscosity.
- Resistivity: $\Delta t_5 = \Delta j^2 / (4\eta)$, where η is the resistivity.

The index j presented above indicates which direction of the adopted coordinate system is being used. Additionally, in order to keep radial zones coupled after each step, a new time limit Δt_{shear} is computed and is related to the shear, which is important in case the other limits are larger:

$$\Delta t_{shear} < C_0 \left(\frac{V_x(i,j,k)}{\Delta X_j} - \frac{V_x(i,j+1,k)}{\Delta X_{j+1}} \right)^{-1} \tag{2.27}$$

The transport step has a common problem regarding azimuthal velocities with large and uniform values. For that purpose, the orbital advection technique is employed on the transported variables, similar to what was implemented in the original FARGO code. [51] It basically consists of breaking down the azimuthal velocity, located inside a given radius and height, into two parts: a larger, constant velocity (v^0), and a smaller, residual one (∂v):

$$v = v^0 + \partial v \tag{2.28}$$

The transport is then solved in two phases by operator splitting technique, each assuming a different velocity, leading to a circular permutation of indices and conservative updates, therefore conserving these fields to machine accuracy. [52]

The total azimuthal velocity V_φ in the minimum Δt_2 at step 6, related to fluid motion, must be substituted by ∂v. Considering that obtaining the maximum time frame is a high-priority process in a full cycle, and since it requires the bulk azimuthal velocity for the orbital advection, ∂v is calculated early in the full update, at step 3 of Figure 2.2.

The implementation of planets as point-like bodies interacting with the gas is present in the FARGO3D code by the fifth-order Cash–Karp method, [59] processed at substep 5a of Figure 2.2 by calculating the planet velocities under the influence of the gas force. Such operation can be either executed by summing up the contributions to the force coming from all cells, or by removing the axisymmetry from the gas density. The method consists of solving the differential equation $dy/dt = f(t, y)$, where y is a 6-vector with three-dimensional position and velocity, for each of the N number of planets. The approximated solution is:

$$y^{n+1} = y^n + h \sum_{i}^{6} b_i k_i \tag{2.29}$$

with function k_i as:

$$k_i = f\left(t_n + c_i h,\ y^n + h \sum_{j=1}^{6} a_{ij} k_j \right) \tag{2.30}$$

where n index is the iteration number, h is the step length, and coefficients a, b, c are represented by the standard Butcher table, as expressed by Cash & Carp in their work. [59] Unfortunately, the method brings limitations in what concerns to close encounters that can only be overcome by including an adapted time step disconnected from the CFL condition, which on the other hand is decoupled from the planet interactions.

2.2 MULTIFLUID IMPLEMENTATION

Starting from the base FARGO3D, Llambay et al. [54] developed an extra feature that includes dust populations in the numerical method, as a tool for the study of dust evolution in circumstellar disks. Therefore, it will be of great importance for the research development on gap formation by outward migrating planets, as proposed in this dissertation.

The code assumes the temperature with only spatial dependence and no mass transfer between dust species. Furthermore, it takes in a number N of dust size population, and develops the evolution of the system by applying on each one of them separately the hydrodynamical equations of density and momentum conservation (Eqs. 2.1 and 2.2). It also adopts the operator splitting method as discussed in the past section. The collision terms, instead, are addressed in an extra substep in the source step by solving the approximate form:

$$\frac{\partial v_i}{\partial t} = \frac{F_i}{\rho_i} \tag{2.31}$$

The drag force per unit volume, F_i, is:

$$F_i = -\rho_i \sum_{j \neq i} \alpha_{ij}(v_i - v_j) \tag{2.32}$$

where subscripts represent a given population and α_{ij} is the collision rate between the two species represented in its index. When it comes to a multifluid scenario, the time step is restricted in case of large collision rates, therefore a implicit solution of the Eq. 2.31 is important. Starting by writing it in finite differential form:

$$v_i^n = v_i^{n+1} \left[1 + \Delta t \sum_{j \neq i} \alpha_{ij}^n \right] - \Delta t \sum_{j \neq i} \alpha_{ij}^n v_j^{n+1} \tag{2.33}$$

which can be also formulated as a matrix equation:

$$V_k = [v_1 \cdot e_k, \ldots, v_N \cdot e_k]^T \tag{2.34}$$

$$V_k^n = T V_k^{n+1} \tag{2.35}$$

where V_k is composed by the velocity projection v_N of the N-th species along the direction of the unit vector e_k. T is a N x N matrix given by:

$$T = I + \Delta t M \tag{2.36}$$

with I as the identity matrix and M as the matrix:

$$M_{ij} = \sum_{k \neq i}^{N} \alpha_{ik}^{n} \delta_{ij} - \alpha_{ij}^{n}(1 - \delta_{ij}) \tag{2.37}$$

where the first term delineates the diagonal entries, in opposition to the non-diagonal values from the second term. Eq. 2.35 is solved numerically by Gaussian elimination with partial pivoting. [60] The algorithm approach on the implicit scheme assures momentum conservation to machine precision and asymptotic stability (i.e., the ability to reach an equilibrium solution from the initial conditions after any given time step Δt).

The code does not actually encompass the collision rate α_{ij} as the explicit interaction between dust populations, but rather adopts an indirect calculation between the dust species and the gas, as follows:

$$\alpha_{ij} = \alpha_i \delta_{jg} + \varepsilon_j \alpha_j \delta_{gi} \tag{2.38}$$

$$\alpha_i = \frac{\Omega_k}{Ts, i} \tag{2.39}$$

where g index represents the gas, $\varepsilon_j = \rho_j / \rho_g$, and δ_{gi} is called Kronecker delta; Ω_k is the local Keplerian frequency, and T_s is the Stokes number which depends on the properties of the gas and dust (in this algorithm, T_s is constant and independent of fluid velocities). The Stokes number is an useful quantity to identify dynamical coupling of particles; materials with same number show the same behavior. It is defined by the dimensionless $T_s = \Omega_K \tau_s$. It is basically represented by the ratio between the orbital period (Ω_K) and friction time, or stopping time, which is the characteristic timescale of (de)acceleration of a specific population, given by $\tau_s = mv/F_D$ (F_D is the drag force). [61]

The insertion of the implicit approach in the code is described by the flowchart in Fig. 2.3. The collisional step is included between the source and transport in order to assure that the motion between gas and dust does not achieve the asymptotic limit of the terminal velocity, which would not be possible if implemented before and after these two original steps. An extra predictor step can also be called right before the source, whenever this step depends on velocities. It will settle a partial velocity by collision operations ($V^{n+1/2}$) at half-time step $\Delta t/2$. The updated velocity will then be taken to the source, following the regular script.

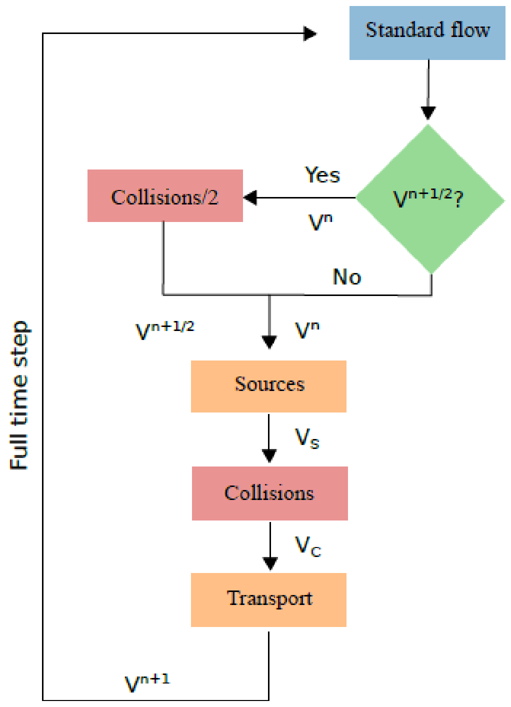

Figure 2.3: Implementation of the multifluid feature in the FARGO3D code, as described by Llambay et al. [54]

2.3 SIMULATION SETUPS

The simulation elaborated by Marzari et al. [1], as much as the one proposed here in this thesis, processes the temporal evolution of the dust and gas density profile along a two-dimensional polar grid in the radial distance and the azimuthal angle (r, φ). They both take into account the specific case of a massive planetary pair that evolves into an outward migration, locked in 2:1 resonance (additionally also in the 3:2 for the run performed by Marzari et al.). Here, the individual setups adopted by each model are discussed, reminding that the goal is to increment with the effects of diffusion and back reaction not embraced by the former work.

2.3.1 NO DIFFUSION AND BACK-REACTION SETUP

Utilizing the original FARGO code from Masset [51], Marzari et al. [1] settled a total number of 4×10^5 particles, and separated the dust into four groups of size populations: 100 μm, 10 μm, 1 mm, and 1 cm. The disk is placed over a 720 x 360 grid with an enclosed radius ranging between 0.5 and 15 AU. Its density profile is expressed as:

$$\Sigma(r) = \Sigma_0 \left(\frac{r}{AU}\right)^{-p} g \cdot cm^{-2} \tag{2.40}$$

with initial density and power index values differing according to the resonance: Σ_0 = 750 or 1000 gcm^{-2}, and $p = 1$ for the 3:2 MMR; Σ_0 = 750 gcm^{-2} and p = 3/2 for the 2:1. The shear kinematic viscosity is given by $\nu = \alpha H^2 \Omega$, with Ω as Keplerian frequency of the disk; the turbulence parameter constant as α = 10^{-4} or 10^{-3} for the 3:2 MMR, while α = 10^{-4} for the 2:1. The disk aspect ration ($h = H/r$) is as small as 0.02.

The conservation of energy, in a Lagrangian approach, is set to include the viscous heating and radiative cooling through the disk surface:

$$\frac{\partial E}{\partial t} + \nabla \cdot (E u) = -P \nabla \cdot u + Q^+ - Q^- \tag{2.41}$$

where E and P are the total surface density of energy and pressure, respectively, and u is the gas velocity field. Q^+ is the viscous dissipation term, which incorporates the physical kinematic viscosity and the von Neumann-Richtmyer artificial bulk viscosity, [62] and where the coefficient defining the number of zones over which shock fronts are smeared out is set to 1.41. $Q^- = 2\sigma_{SB} T_{eff}^4$ is the local radiative cooling; the effective temperature T_{eff} is based on Bell & Lin's work. [63]

The drag force is modeled after Picogna & Kley's work [64]:

$$F_D = (1-f)F_{D,E} + fF_{D,S} \tag{2.42}$$

$$F_{D,E} = -\frac{4}{3}\pi s^2 \rho_g v_{th} v \tag{2.43}$$

$$F_{D,S} = -\frac{1}{2}\pi s^2 C_D \rho_g v_{th} v \tag{2.44}$$

where $F_{D,E}$ and $F_{D,S}$ are respectively the Epstein and Stokes drag, s is the spherical radius of the solid particle, v_{th} and ρ_g are respectively the thermal velocity and density of the gas molecules; C_D is the drag coefficient whose value depends on the Reynolds number, $Re = 2s\rho v/\eta$, with η being the gas viscosity; [65] f is a coefficient that dictates the transition between both drag regimes:

$$f = \frac{s}{s+\lambda} = \frac{1}{1+Kn} \tag{2.45}$$

where λ is the mean free path of the gas molecules and s is the particle radius; $Kn = \lambda/s$ is the Knudsen number and expresses the influence of inter-molecular collisions. If $Kn \ll 1$, inter-molecular collisions are frequent and the stream of gas particles colliding with the dust grain becomes viscous.

The drift velocity of the dust in relation to the gas, due to drag forces, is:

$$v_{drift} = \frac{1}{St^{-1} + St} \left(\frac{\partial P}{\partial r} \right) \frac{1}{\rho_g \Omega} \tag{2.46}$$

with St as the Stokes number. Further calculations were done on orbital advection as employed by D'Angelo & Marzari, [39] and their results will also be discussed in the next section.

2.3.2 Diffusion and back-reaction setup

This time the code adopted is FARGO3D. The inner planet has Jupiter's mass, while the outer one has Saturn's. The following properties are adopted: same aspect ratio of the cold disk, $H/r = h = 0.02$; shear kinematic viscosity, in terms of $H^2\Omega$, is 10^{-7}; dust species are separated into 100 μm, 1 mm and 1 cm sizes; disk extension goes from 0.4 to 12 AU. Surface density is defined as in the past setup (Eq. 2.40), but with initial sigma $\Sigma_0 = 4 \cdot 10^{-6}$ $M_\odot/AU^{-2}$ ($\sim$35.55 gcm^{-2}) and power law index $p = 1$; dust-to-gas ratio is 0.003; disk distributed in a grid of 1024 x 512.

The drag force of the gas density on the dust particles here follows the approach of Woitke & Helling [66]:

$$F = \left(\frac{3K}{3K+1} \right)^2 F_E + \left(\frac{1}{3K+1} \right)^2 F_S \tag{2.47}$$

with K as the Knudsen number. F_E is the Epstein drag:

$$F_E = -\frac{4}{3} \left(1 + \frac{9\pi}{128} M^2 \right)^{1/2} s^2 \rho_g v_{th} v_{rel} \tag{2.48}$$

and F_S is the Stokes drag:

$$F_S = -\frac{1}{2} C_D \pi s^2 \rho_g v_{th} v_{rel} \tag{2.49}$$

where ρ_g is the gas density, s is the particle radius, v_{th} and v_{rel} are, respectively, the local thermal velocity and the relative velocity of the gas particles (in relation to the dust), and M is the Mach number obtained from v_{rel}.

To be able to include the diffusion in the dust model, the following new term was added to the continuity equation: [67]

$$\frac{\partial \rho_d}{\partial t} = \nabla \cdot \left(D\rho_t \nabla \frac{\rho_d}{\rho_t} \right) \tag{2.50}$$

where $\rho_t = \rho_g + \rho_d$ is the sum of the gas and dust densities, and D is the diffusion coefficient (same value for both fluids). Here, the original code from Llambay et al., which keeps the Stokes number as a constant according to the properties of the fluids, is modified to make the same number depend on dust particle size instead.

3

Results

Having the purpose and the model of the research already established, we now expose the main results of the aforementioned simulations, focusing on the 2:1 resonance scenario. The outcome of Marzari et al. [1] is presented in the first subsection, followed by the results of my own simulation, in order to allow us to compare the differences and interpret the impact of diffusion and back-reaction on the gap formation.

3.1 No diffusion and back-reaction run

Fig. 3.1 shows the evolution of the semi-major axis and eccentricity along a time fraction of nearly 50 kyr from the total protoplanetary system life span, for both the 2:1 and 3:2 resonances. The inner heavier and the outer lighter Jovian planets exhibit the initial inward migration, which is then reverted outwards after capture. This process is much more intense for the 3:2. In contrast, for the 2:1, the inner planet starts straight from the outward motion. This is attributed by Marzari et al. to the tidal interactions with the gas, which induce eccentric perturbations in the disk, producing a positive torque on the planet. [68] The results are in good agreement with the Equation 1.28, which confirms the 2:1 resonance captures for surface densities as low as 40 gcm^{-2} at r ∼6 AU.

As predicted, eccentricities also escalate with haste from the approximately circular orbits after the resonance is established. Although, not much changes for the inner planet in the 3:2

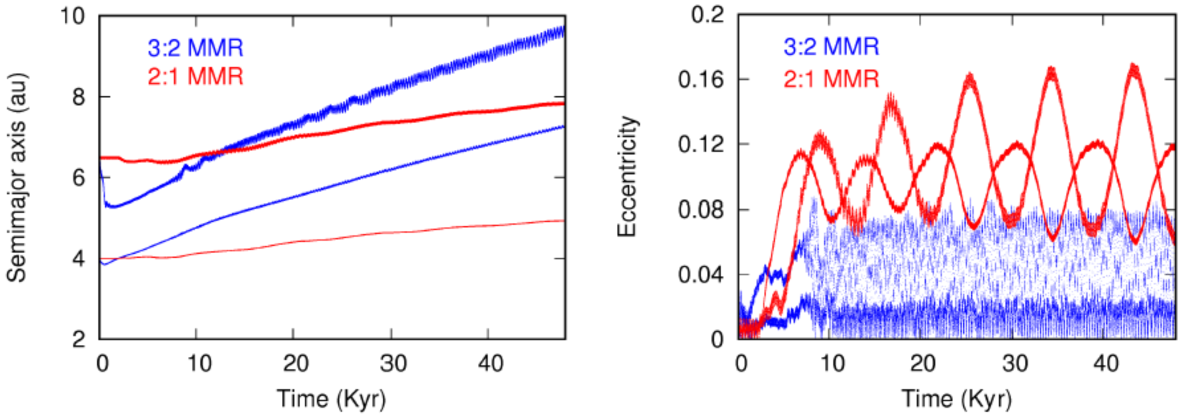

Figure 3.1: Evolution of semi-major axis and eccentricity for both the 2:1 and 3:2 resonances. [1]

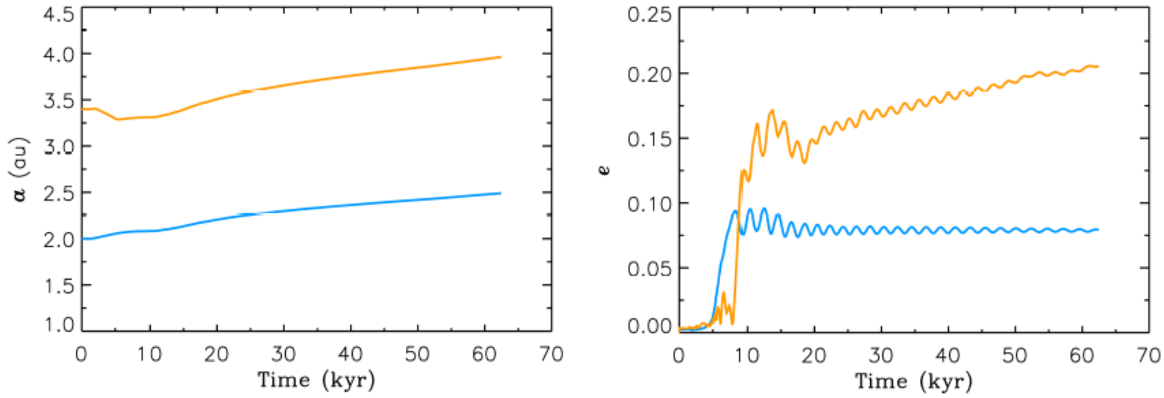

Figure 3.2: Evolution of semi-major axis and eccentricity in the scenario of 2:1 resonance capture, [1] adopting the orbital advection code implementation from D'Angelo & Marzari. [39]

resonance, while the outer one stabilizes around 0.05. As for the 2:1 ratio, the planets maintain a wide oscillation between 0.07 - 0.12 and 0.07 - 0.16.

An additional simulation was performed for the 2:1 using the orbital advection algorithm implemented in FARGO3D, as proposed by D'Angelo & Marzari. [39] It integrates the equations of motion with the background orbital motion removed, greatly increasing the efficiency of the algorithm by increasing the time step. The following disk configurations were employed: kinematic viscosity $\nu = 4 \times 10^{-8}$ in units of Ωr^2 and turbulence parameter $\alpha = 10^{-4}$, both at 1 AU; surface density Σ_0 = 530 gcm^{-2} and power law index $p = 3/2$ (see Eq. 2.40); flared, locally isothermal disk with $H/r = 0.024(r/AU)^{2/7}$, and radius extending from 0.25 to 54 AU.

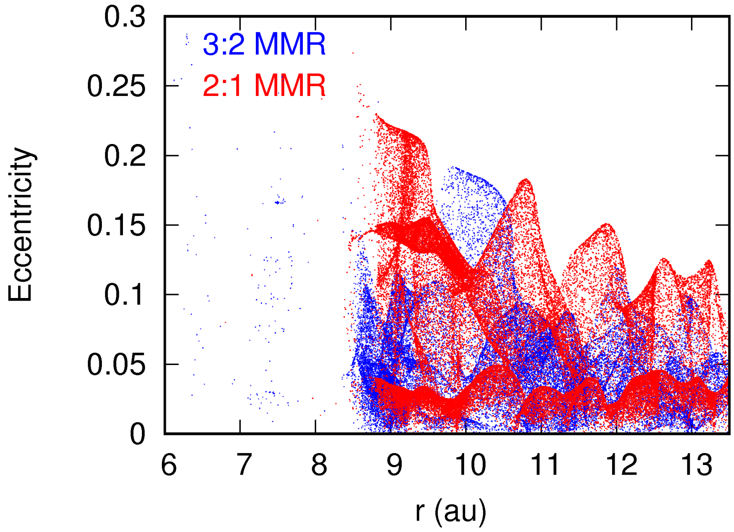

Figure 3.3: Eccentricity of dust particles along the disk radius for both the 2:1 and 3:2 resonances. [1]

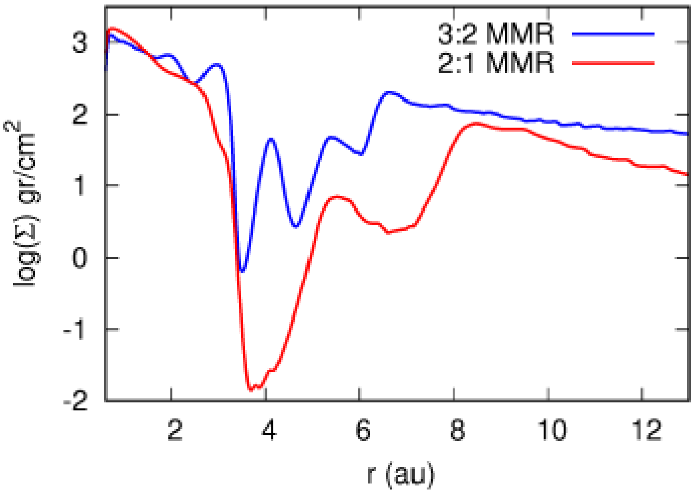

Figure 3.4: Surface density distributions along the disk radius for both the 2:1 and 3:2 resonances. [1]

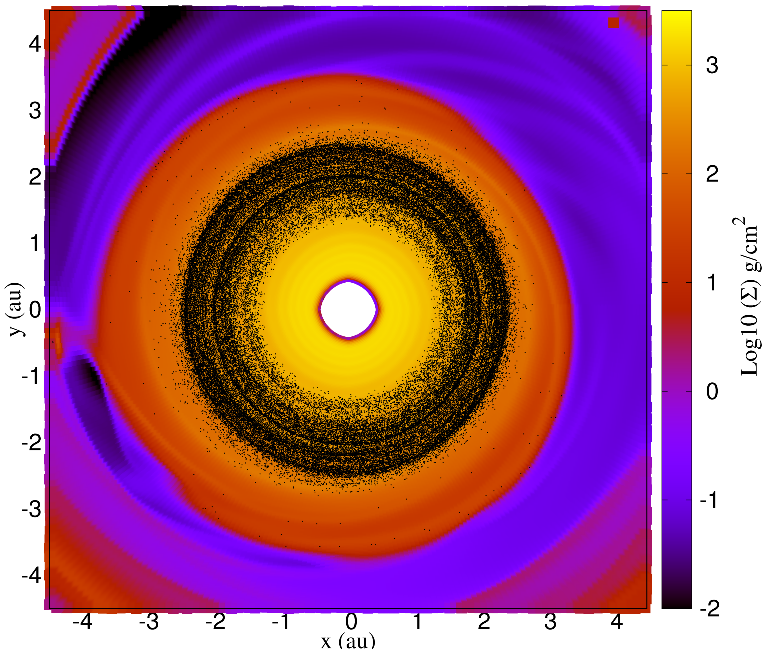

Figure 3.5: Surface density distribution in Cartesian coordinates of the inner disk after 30 kyr of outward migration of the planetary pair in a 2:1 resonance. Dust particles of 10 μm are represented by black dots. [1]

Again, as exposed by Fig. 3.2, a reverted inward to outward motion can be noted at least for the lighter planet, while the more massive one starts from the outward trajectory. Eccentricities also have a sharp rise; the inner planet is soon stabilized around 0.08, but the outer one follows a slight ascension towards 0.2. The results are also in agreement with Eq. 1.28 and are similar to the first run, implying that the disk structure does not interfere directly with the migration as long as it is cold and not much viscous. Marzari et al. add that the large eccentricity oscillations from the first run, larger than in the second, are likely a consequence of the difference in aspect ratio (H/r), and the addition of a locally isothermal setup in which the disk temperature is not affected by kinematic viscosity. [68]

The planetary eccentricities also have an impact on the dust. Figure 3.3 illustrates the eccentricity of particles for both MMR. The 2:1 is represented by a time frame ahead of the 3:2, in order to match the positions of the dust and gas gaps. Like the planets, particles in the 2:1 case reach higher values than in the counterpart resonance.

Figure 3.4 shows the resulting surface density along the radius for both resonance ratios. The 2:1 MMR shows a wider and deeper gap in relation to the 3:2. This particular width is connected to the shorter distance between planets and larger eccentricity changes as described before. The depth is linked to the slower migration speed instead. The lock into 2:1 is due to

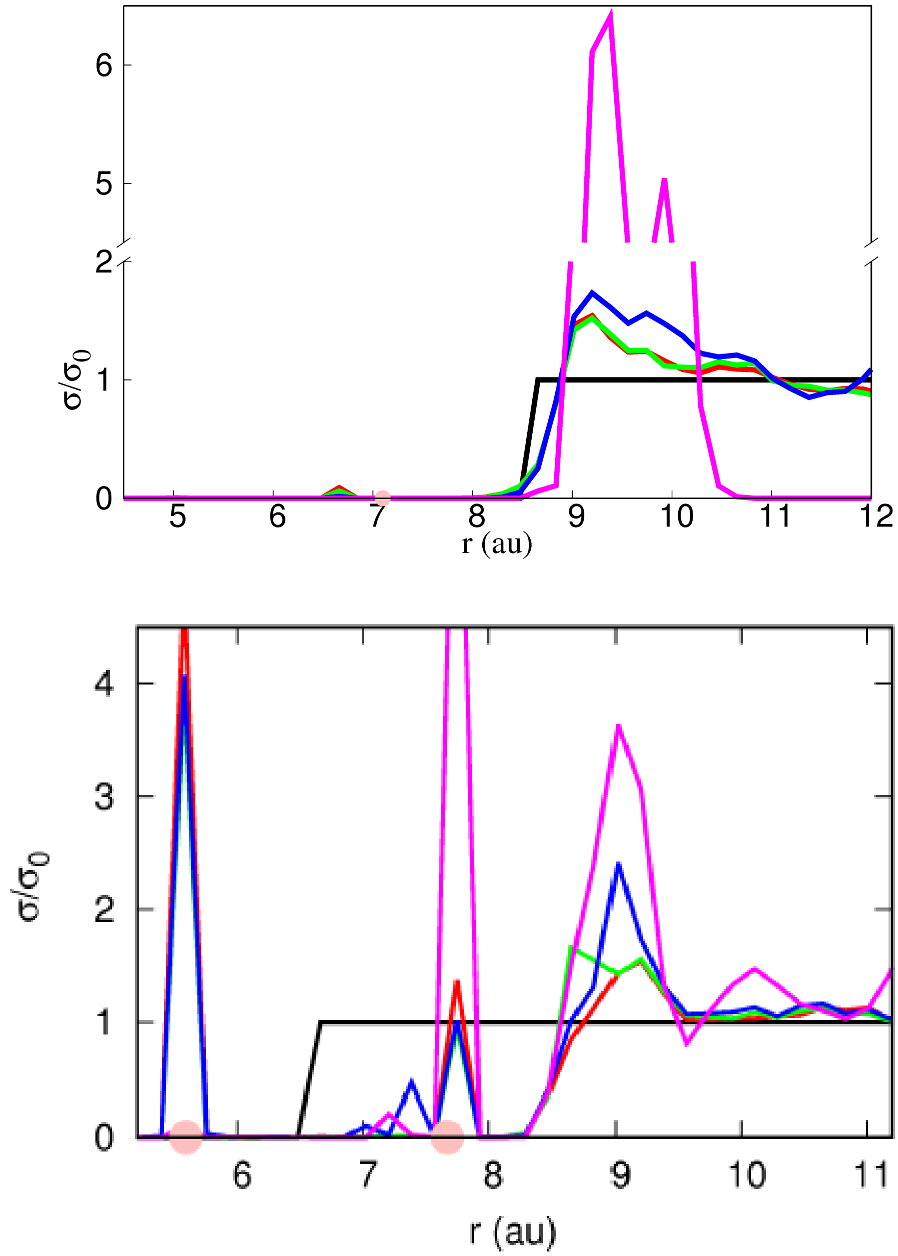

Figure 3.6: Histograms of dust distribution. Top: 30 kyr after the simulation start with the 2:1 resonant capture. Bottom: 20 kyr after the simulation start with the 3:2 resonance capture. The black line indicates the initial distribution of dust while the red, green, blue and magenta lines represent the distribution of 10 μm, 100 μm, 1 mm, and 1 cm sized particles, respectively. Densities in the vertical axis are in terms of the initial value σ_0. [1]

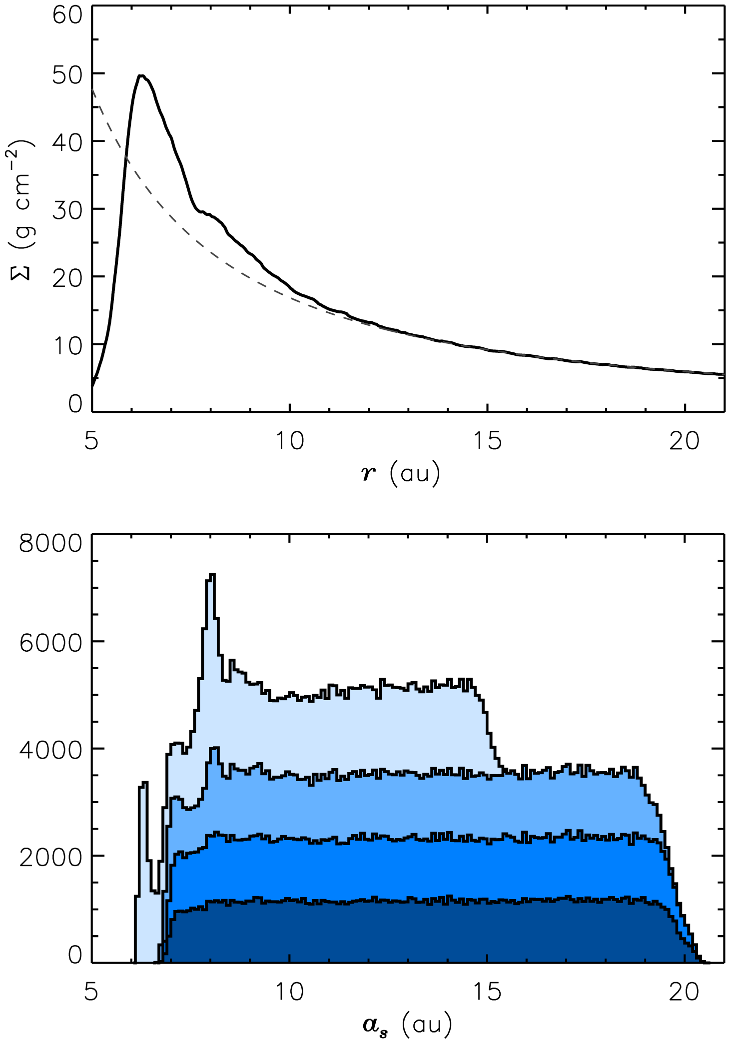

Figure 3.7: Top plot shows the azimuthally averaged gas surface density in the outer disk, with the dashed line as the initial distribution. Bottom diagram is a histogram, 2 kyr after the planet migration, with the number of specimens by disk radius of four different dust populations, respectively from dark to light blue shades: 10 μm, 100 μm, 1 mm, and 1 cm. [1]

the power law index $p = 3/2$ which, according to Eq. 2.40, entails a lower density if compared to $p = 1$ employed in the 3:2 MMR.

Figure 3.5 plots the inner disk density distribution in Cartesian coordinates after 30 kyr, with dust particles of 10 μm represented by black dots. Marzari et al. observe that, during the proposed time scale, the dust component is not resupplied by the outer disk anymore and starts receding from the gas. The dust also tends to have a progressively broader gap compared to the gas, the latter refilling the empty space left by the former. This phenomenon takes longer for the 2:1 resonance, also thanks to its slower migration.

A histogram of the dust distribution in the outer disk is displayed in Fig. 3.6, with densities separated into four particle size populations: 10 μm, 100 μm, 1 mm, and 1 cm. It is possible to note that, for the 2:1, all the dust species are well contained outside the over-density in the outer border of the gap. Such trapping efficiency is not found in the 3:2 case.

The locally isothermal setup is put to use again in Fig. 3.7, now with a much shorter time frame of 2 kyr. With the migrating planets located at around 2.5 and 3.97 AU, the top panel exhibits the gas distribution of the external disk. The bottom one presents the dust demography by number of particles along the radius, spread evenly at the beginning of the simulation within the radial range of 7 to 20 AU. The Stokes numbers here range from 10^4 (for the smallest particles) to the order of 10^2 (for the largest particles). Remarkably, larger dust particles tend to flow inwards in more quantities than smaller ones, but they are all impeded by the gas peak around 7 AU. The lower over-density in relation to the first run is due to the lower surface density Σ, which is expected to be overcome with further evolution time frame.

3.2 DIFFUSION AND BACK-REACTION RUN

This time, the setup with the diffusion and back-reaction interactions is employed. Kinematic viscosity and surface density distribution are kept remarkably low, as expected from a disk with planets in its late evolution. It is also important to remind that the 2:1 locking requires lower densities if compared to the 3:2, and lower viscosity produces shorter outward migrations. The estimated eccentricity and semi-major evolution of the planetary pair in 2:1 MMR are depicted in Figure 3.8, distributed along a time frame of $\sim$46 kyr. Again, the eccentricities assume a sharp rise from the beginning of the capture, then oscillate between 0.07 - 0.09 and 0.07 - 0.12, respectively for the inner and outer planets. In parallel, the planets display a very modest migration rate, as expected. They go initially inwards and then outwards, with semi-major axis fluctuating around 3.95 - 4.0 for the inner planet and 6.2 - 6.4 for the outer one.

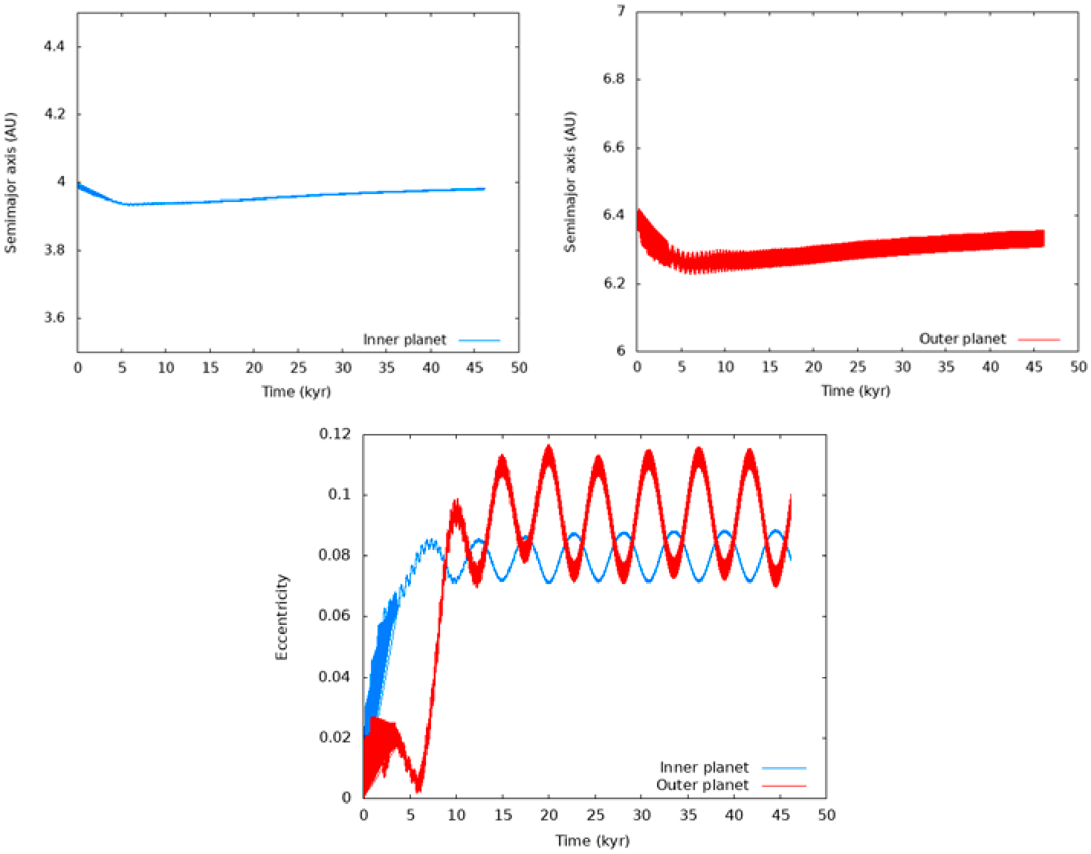

Figure 3.8: Left and right panel describe the semi-major axis evolution for the inner and outer planets, respectively for the 2:1 resonance. Bottom plot exhibits the eccentricity of the same pair. Time scale in both cases is ∼46 kyr.

The dust distribution for the three dust species along the azimuthal angle by the external disk radius is shown in Figure 3.9. The same time frame of ∼46 kyr is employed. Quite apparent is the fact that the bigger the particle size, the more depleted its population inside the disk, at least when it comes to the distribution along the radius. Looking from the 100 μm to the 1 mm diagrams, it is possible to note that the ring starts to dissolve into clumps. Then moving to the 1 cm, it becomes limited to very small and thick blobs at ∼7.5 and 9 AU, away from the planet positions. Curiously enough, the inner edge of the dust gap can still be observed for the 100 μm species at 2 AU.

Figure 3.10 shows the same kind of density map but this time using the gas instead. The gap here is much more uniform than the dust's, with a regular vertical distribution. The inner edge is also clearly more prominent and shows some decoupling from the solids, but the outer border limits of both gas and the 1 cm particles seem to match closely with each other.

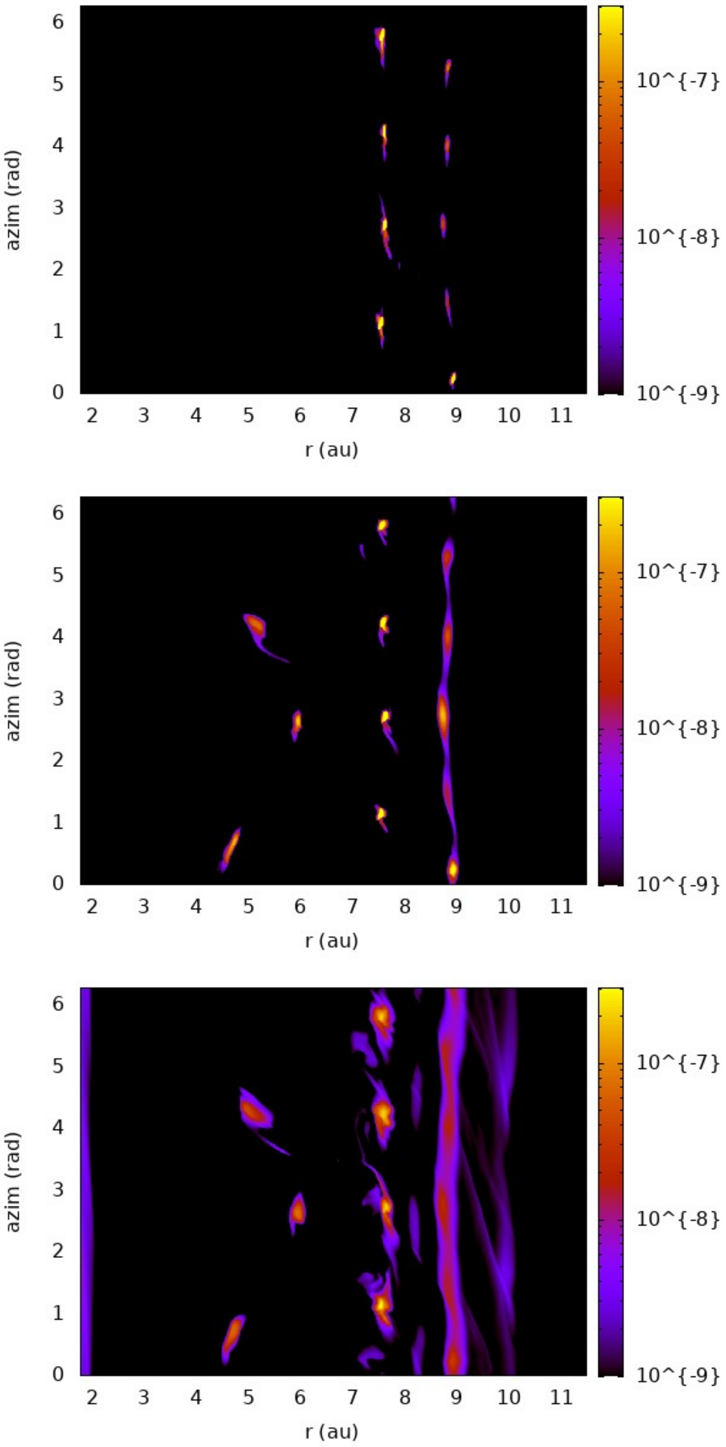

Figure 3.9: Dust density maps of the 1 cm, 1 mm, and 100 μm particle size populations, respectively from top to bottom panels, for the 2:1 planetary resonance. Spatial coordinates are the disk radius by azimuthal angle, with density represented by color gradient.

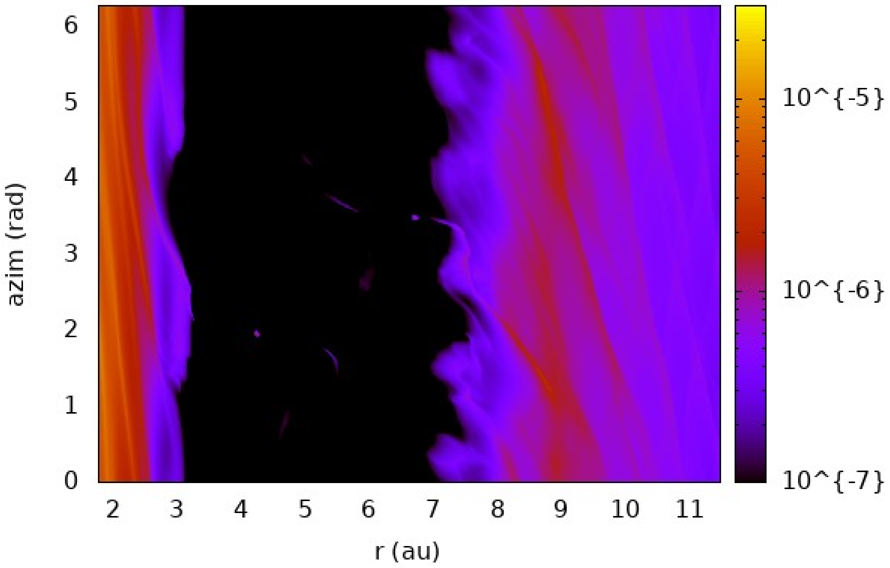

Figure 3.10: Gas density map for the case of a 2:1 planetary resonance, plotted along the disk radius by azimuthal angle coordinates, with density represented by color gradient.

Lastly, figure 3.11 displays the surface profile of all populations, including the gas. Clearer than before, it is possible to notice the over-density right at the outer edge of the gap, located outside by the less massive planet's orbit. Inside the maximum, all dust populations are represented, but the highest peak is of 1 cm particles. The density follows a proportional trend in relation to dust size. The over-density blocks all the particles from crossing the edge with efficiency, except for the 1 mm and 100 μm species which can be found between the orbits of the planetary pair. Again, the decoupling of inner edges between the gaps can be distinguished with a difference of approximately 1 AU. A second, less marked peak can be observed after the outer border where all dust population densities are mostly comparable, but this time with a slight trend that is inversely proportional to particle size. The gas at the outer disk extends from the over-density to beyond the 12 AU frame without big spikes, its maximum coinciding with the second highest dust peak.

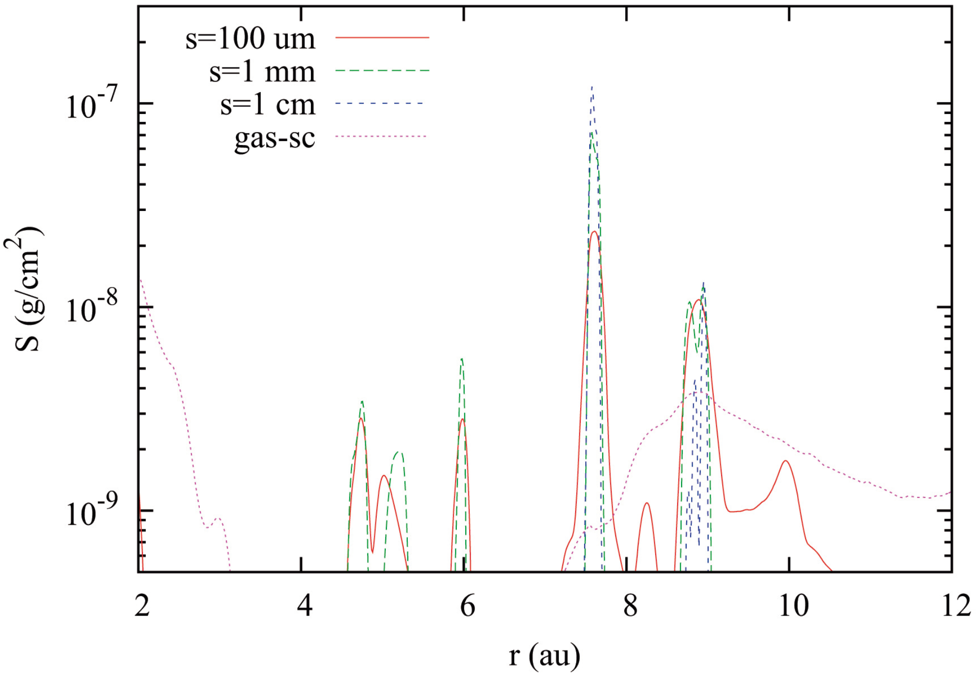

Figure 3.11: Surface density profile for the three dust size populations (100 μm, 1 mm and 1 cm) and the gas.

4

Discussion

With all the necessary results laid down, it is now possible to compare the output of both setups and infer about the impact of diffusion and back-reaction on the dust distribution around two planets in resonance migrating outwards.

Starting with the conclusions of Marzari et al., [1] as observed by them, the gap decoupling is one of the unique features of outward migrating planets, in comparison with single planets or a pair in an inward motion only. A bigger hole is carved in the dust than in the gas since the solids do not migrate inwards from the outer disk to fill up the vacant space which is increasing because of the outwards migration, while the gaseous gap keeps its shape and moves up with the planets since the gas is able to filter through the gap. This process differs according to the MMR outward migration rate since the timescale of evolution is slower for the 2:1 than for the 3:2. Furthermore, the two resonances cause a different eccentricity evolution of the planets and of the dust particles which, in the case of the 2:1 resonance, cause a widening of the gap.

Another sign of outward migration is the presence of an over-density in the dust distribution at the external gap edge, where a higher abundance of larger dust particles accumulates because of the dust trap. This structure can be observed in high-resolution images by the presence of a luminous ring, and also has peculiarities according to MMR rate. The slow evolution of the 2:1 resonance induces more efficient retention of dust compared to the 3:2, preventing solids from reaching the planets.

In theory, disk properties barely affect the outward migration in a 2:1 resonance as long as low temperature and viscosity are adopted. This choice is reasonable due to the advanced age of the disk which needed time to form the two giant planets. Nonetheless, the effects of diffusion due to turbulence of the gas on the dust particles are supposed to weaken the strength of the dust trap by allowing grains to filter through the trap at the outer edge.

Furthermore, the dust back-reaction on the gas, especially inside the over-densities where the dust-to-gas ratio is increased, might cause structural changes on the dust trap. Marzari et al. acknowledged not addressing this effect in their calculations and warned that further investigations should take place.

Due to the potential relevance of both back-reaction and diffusion, I now focus on the outputs from my own simulation setup. Starting from the semi-major axis evolution shown in Figures 3.1 and 3.8, it is noteworthy that both cases follow the same trend. There are some differences in the orbital evolution of the planets and in the gap structure, possibly due to different values of kinetic viscosity and surface density, which are lower for the second setup. This is related to the different numerical models. In the first setup, a full radiative disk was adopted while in the multi-fluid model an isothermal approximation is used (it is the only available in the code).

Comparing Figures 3.6 and 3.11, it is possible to see that, for the 2:1, the dust trap still remains quite prominent from one case to other, with a tall bump in both scenarios. The discrepancy resides in the apparent decrease in efficiency, as one can observe small but considerable piles of 1 mm and 1 μm in the second scenario (also observed in Fig. 3.9). In the first simulation, the same kind of lump can also be observed, but of very negligible proportions. As elaborated by Rice et al., [26] pressure gradients can also act as filters by allowing particles smaller than some critical size to cross the border. The size threshold will depend on the stellar accretion mass, viscosity parameter α and planetary mass. According to Zhu et al.'s simulations, [47] for a disk with $\alpha = 0.01$, $\dot{M} = 10^{-8}\ \mathrm{M}_{\odot}\ \mathrm{yr}^{-1}$, and a planet with few Jupiter masses, the limit can be around 100 μm. This filtration will eventually segregate populations, with smaller particles in the inner disk and bigger ones in the outer region. The presence of diffusion and back-reaction proves to affect the efficiency of the dust trap, and as consequence, the filtering will come up more evident.

The results of the second setup are also in agreement with Equation 1.28 by a small margin, for the initial surface density $\Sigma_0 = 4.0 \times 10^{-6}\ \mathrm{M}_*/\mathrm{AU}^2$ at 6.4 AU.

5

Conclusion

I have performed a hydrodynamical, two-dimensional simulation of a protoplanetary disk with a pair of planets embedded in it. The system includes one point-like body as massive as Jupiter in the inner orbit, and another with Saturn's mass in the outer radius. The initial conditions were chosen in order to have convergent migration of the two planets until they are trapped in a 2:1 resonance. After the capture, due to the formation of a common gap in the gas distribution around the two planets, the planets reverse their migration which is now outwards. I have adopted the FARGO3D code [52] in the $rx\varphi$ coordinates with the multi-fluid implementation by Llambay et al. [54] which allowed to model the evolution of the gas and the dust particles treated as a pressureless fluid. I have considered three different populations of dust particle with sizes 1 cm, 1 mm, and 100 μm, respectively. Furthermore, in the code the effects of the gaseous turbulent motion, which causes a diffusion of the dust, and the back-reaction of dust on the gas are included. The main goal of my study was to further develop the simulations conducted by Marzari et al., [1] which adopted the same protoplanetary scenario in both 2:1 and 3:2 resonances, but did not add the effects of dust diffusion and feedback, as stated by the authors.

Comparing the density profiles of the three dust particle populations for the 2:1 resonance without diffusion and back-reaction (Fig. 3.6, top panel) and those coming out from new simulation with the two effects included (Fig. 3.11, top panel), a small decrease in efficiency in the dust trap can be noticed. With the inclusion of the two new effects in the code, the trap became less sensitive to the two smallest particle sizes and a small amount of dust is able to filter through the gap into the inner part of the disk. Regardless, those peculiarities were not strong enough to significantly undermine the over-density formation.

We, therefore, conclude that gas turbulence and back-reaction do impact the morphological evolution of the dust distribution in the disk but not at such an extent to erase the features marking the presence of the two planets in resonance. The characteristic features in the dust caused by the planetary outward migration, i.e., the inner hole and the peak at the outer edge of the common gap, are still present and, once detected by high resolution images, may be used as diagnostic of the presence of the two planets. Thus, to precisely evaluate the relevance of the phenomena, it is recommended to include in the simulations both diffusion and back-reaction.

References

[1] F. Marzari, G. D'Angelo, and G. Picogna, "Circumstellar dust distribution in systems with two planets in resonance," *The Astronomical Journal*, vol. 157, no. 2, p. 45, jan 2019.

[2] P. J. Armitage, *Astrophysics of Planet Formation*. Cambridge University Press, 2009.

[3] J. P. Williams and L. A. Cieza, "Protoplanetary disks and their evolution," *Annual Review of Astronomy and Astrophysics*, vol. 49, pp. 67–117, 2011.

[4] C. J. Lada, "Star formation: from OB associations to protostars." in *Star Forming Regions*, vol. 115, Jan. 1987, p. 1.

[5] P. Andre, D. Ward-Thompson, and M. Barsony, "Submillimeter Continuum Observations of rho Ophiuchi A: The Candidate Protostar VLA 1623 and Prestellar Clumps," *Astrophysical Journal*, vol. 406, p. 122, Mar. 1993.

[6] T. P. Greene, B. A. Wilking, P. Andre, E. T. Young, and C. J. Lada, "Further Mid-Infrared Study of the rho Ophiuchi Cloud Young Stellar Population: Luminosities and Masses of Pre–Main-Sequence Stars," *The Astrophysical Journal*, vol. 434, p. 614, Oct. 1994.

[7] M. Barsony, "Class 0 Protostars," in *Clouds, Cores, and Low Mass Stars*, ser. Astronomical Society of the Pacific Conference Series, vol. 65, Jan. 1994, p. 197.

[8] T. Birnstiel, H. Klahr, and B. Ercolano, "A simple model for the evolution of the dust population in protoplanetary disks," *Astronomy & Astrophysics*, vol. 539, p. A148, mar 2012.

[9] Birnstiel, T., Dullemond, C. P., and Brauer, F., "Gas- and dust evolution in protoplanetary disks," *Astronomy & Astrophysics*, vol. 513, p. A79, 2010.

[10] S. M. Andrews and J. P. Williams, "Circumstellar dust disks in taurus-auriga: The submillimeter perspective," *The Astrophysical Journal*, vol. 631, no. 2, pp. 1134–1160, oct 2005.

[11] S. M. Andrews, D. J. Wilner, A. M. Hughes, C. Qi, and C. P. Dullemond, "Protoplanetary disk structures in ophiuchus," *The Astrophysical Journal*, vol. 700, no. 2, pp. 1502–1523, jul 2009.

[12] ——, "Protoplanetary disk structures in ophiuchus. ii. extension to fainter sources," *The Astrophysical Journal*, vol. 723, no. 2, p. 1241, oct 2010.

[13] A. M. Hughes, D. J. Wilner, C. Qi, and M. R. Hogerheijde, "Gas and Dust Emission at the Outer Edge of Protoplanetary Disks," *The Astrophysical Journal*, vol. 678, no. 2, pp. 1119–1126, May 2008.

[14] D. Hollenbach, D. Johnstone, S. Lizano, and F. Shu, "Photoevaporation of Disks around Massive Stars and Application to Ultracompact H II Regions," *The Astrophysical Journal*, vol. 428, p. 654, Jun. 1994.

[15] T. Kai, T. Baba, and K. Arai, "An Accretion-Disk Model with Cooling through Molecular Lines," *Publications of the Astronomical Society of Japan*, vol. 64, no. 4, 08 2012.

[16] T. Nakamoto and Y. Nakagawa, "Formation, Early Evolution, and Gravitational Stability of Protoplanetary Disks," *The Astrophysical Journal*, vol. 421, p. 640, Feb. 1994.

[17] S. P. Ruden and J. B. Pollack, "The Dynamical Evolution of the Protosolar Nebula," *The Astrophysical Journal*, vol. 375, p. 740, Jul. 1991.

[18] F. Hersant, B. Dubrulle, and J.-M. Huré , "Turbulence in circumstellar disks," *Astronomy & Astrophysics*, vol. 429, no. 2, pp. 531–542, dec 2004.

[19] T. Takeuchi and D. N. C. Lin, "Radial flow of dust particles in accretion disks," *The Astrophysical Journal*, vol. 581, no. 2, pp. 1344–1355, dec 2002.

[20] S. M. Andrews, "Observations of solids in protoplanetary disks," *Publications of the Astronomical Society of the Pacific*, vol. 127, no. 956, pp. 961–993, oct 2015.

[21] P. Pinilla, T. Birnstiel, L. Ricci, C. P. Dullemond, A. L. Uribe, L. Testi, and A. Natta, "Trapping dust particles in the outer regions of protoplanetary disks," *Astronomy & Astrophysics*, vol. 538, p. A114, feb 2012.

[22] G. Picogna and W. Kley, "How do giant planetary cores shape the dust disk?" *Astronomy & Astrophysics*, vol. 584, p. A110, dec 2015.

[23] G. Dipierro, G. Laibe, D. J. Price, and G. Lodato, "Two mechanisms for dust gap opening in protoplanetary discs," *Monthly Notices of the Royal Astronomical Society*, vol. 459, no. 1, pp. L1–L5, Jun. 2016.

[24] L. Cieza *et al.*, "The spitzer c2d survey of weak-line t tauri stars. ii. new constraints on the timescale for planet building," *The Astrophysical Journal*, vol. 667, no. 1, p. 308, sep 2007.

[25] J. Muzerolle, L. E. Allen, S. T. Megeath, J. Hernández, and R. A. Gutermuth, "A spitzer census of transitional protoplanetary disks with au-scale inner holes," *The Astrophysical Journal*, vol. 708, no. 2, p. 1107, dec 2009.

[26] W. K. M. Rice, P. J. Armitage, K. Wood, and G. Lodato, "Dust filtration at gap edges: implications for the spectral energy distributions of discs with embedded planets," *Monthly Notices of the Royal Astronomical Society*, vol. 373, no. 4, pp. 1619–1626, Dec. 2006.

[27] J. C. Papaloizou and C. Terquem, "Planet formation and migration," *Reports on Progress in Physics*, vol. 69, no. 1, p. 119, 2005.

[28] F. S. Masset, G. D'Angelo, and W. Kley, "On the Migration of Protogiant Solid Cores," *The Astrophysical Journal*, vol. 652, no. 1, pp. 730–745, Nov. 2006.

[29] Paardekooper, S.-J. and Mellema, G., "Dust flow in gas disks in the presence of embedded planets," *Astronomy & Astrophysics*, vol. 453, no. 3, pp. 1129–1140, 2006.

[30] Fouchet, L., Maddison, S. T., Gonzalez, J.-F., and Murray, J. R., "The effect of a planet on the dust distribution in a 3d protoplanetary disk," *Astronomy & Astrophysics*, vol. 474, no. 3, pp. 1037–1047, 2007.

[31] "Exoplanet.eu," http://exoplanet.eu/catalog/, accessed: 2022-09-26.

[32] C. Beaugé, S. Ferraz-Mello, and T. Michtchenko, "Multi-planet extrasolar systems - detection and dynamics," *Research in Astronomy and Astrophysics*, vol. 12, p. 1044, 08 2012.

[33] J. T. Wright and A. W. Howard, "Efficient fitting of multiplanet keplerian models to radial velocity and astrometry data," *The Astrophysical Journal Supplement Series*, vol. 182, no. 1, pp. 205–215, apr 2009.

[34] B. S. Gaudi, "Microlensing Surveys for Exoplanets," *Annual Review of Astronomy and Astrophysics*, vol. 50, pp. 411–453, Sep. 2012.

[35] A. C. M. Correia, J.-B. Delisle, and J. Laskar, "Planets in mean-motion resonances and the system around HD45364," in *Handbook of Exoplanets*. Springer International Publishing, 2018, pp. 2693–2711.

[36] K. Kajtazi, "Capture into mean motion resonance," Master's thesis, Lund University, 2021.

[37] K. M. Deck, M. Payne, and M. J. Holman, "First-order resonance overlap and the stability of close two-planet systems," *The Astrophysical Journal*, vol. 774, no. 2, p. 129, aug 2013.

[38] K. Batygin, "Capture of planets into mean motion resonances and the origins of extrasolar orbital architectures," 2015.

[39] G. D'Angelo and F. Marzari, "Outward Migration of Jupiter and Saturn in Evolved Gaseous Disks," *The Astrophysical Journal*, vol. 757, no. 1, p. 50, Sep. 2012.

[40] C. F. Yoder and S. J. Peale, "The tides of Io," *Icarus*, vol. 47, no. 1, pp. 1–35, Jul. 1981.

[41] C. C. Capobianco, M. Duncan, and H. F. Levison, "Planetesimal-driven planet migration in the presence of a gas disk," *Icarus*, vol. 211, no. 1, pp. 819–831, 2011.

[42] H. Tanaka, T. Takeuchi, and W. R. Ward, "Three-Dimensional Interaction between a Planet and an Isothermal Gaseous Disk. I. Corotation and Lindblad Torques and Planet Migration," *The Astrophysical Journal*, vol. 565, no. 2, pp. 1257–1274, Feb. 2002.

[43] F. C. Adams and A. M. Bloch, "General analysis of type i planetary migration with stochastic perturbations," *The Astrophysical Journal*, vol. 701, no. 2, pp. 1381–1397, jul 2009.

[44] W. Kley and R. Nelson, "Planet-disk interaction and orbital evolution," *Annual Review of Astronomy and Astrophysics*, vol. 50, no. 1, pp. 211–249, sep 2012.

[45] M. Ogihara and H. Kobayashi, "Condition for capture into first-order mean motion resonances and application to constraints on the origin of resonant systems," *The Astrophysical Journal*, vol. 775, no. 1, p. 34, aug 2013.

[46] K. J. Walsh, A. Morbidelli, S. N. Raymond, D. P. O'Brien, and A. M. Mandell, "A low mass for mars from jupiter's early gas-driven migration," *Nature*, vol. 475, no. 7355, pp. 206–209, jun 2011.

[47] Z. Zhu, R. P. Nelson, R. Dong, C. Espaillat, and L. Hartmann, "Dust filtration by planet-induced gap edges: Implications for transitional disks," *The Astrophysical Journal*, vol. 755, no. 1, p. 6, jul 2012.

[48] Schobert, B. N. and Peeters, A. G., "Impact of dust diffusion on the rim shape of protoplanetary disks," *Astronomy & Astrophysics*, vol. 651, p. A27, 2021.

[49] K. D. Kanagawa, T. Muto, S. Okuzumi, T. Tanigawa, T. Taki, and Y. Shibaike, "Impacts of dust feedback on a dust ring induced by a planet in a protoplanetary disk," *The Astrophysical Journal*, vol. 868, no. 1, p. 48, nov 2018.

[50] Taki, Tetsuo, Fujimoto, Masaki, and Ida, Shigeru, "Dust and gas density evolution at a radial pressure bump in protoplanetary disks," *Astronomy & Astrophysics*, vol. 591, p. A86, 2016.

[51] F. Masset, "FARGO: A fast eulerian transport algorithm for differentially rotating disks," *Astronomy and Astrophysics Supplement*, vol. 141, pp. 165–173, Jan. 2000.

[52] P. Benítez-Llambay and F. S. Masset, "Fargo3d: A new gpu-oriented mhd code," *The Astrophysical Journal Supplement Series*, vol. 223, no. 1, p. 11, mar 2016.

[53] "Fargo3d," http://fargo.in2p3.fr/, accessed: 2022-10-29.

[54] P. Benítez-Llambay, L. Krapp, and M. E. Pessah, "Asymptotically Stable Numerical Method for Multispecies Momentum Transfer: Gas and Multifluid Dust Test Suite and Implementation in FARGO3D," *Astrophysical Journal Supplement*, vol. 241, no. 2, p. 25, Apr. 2019.

[55] J. M. Stone and M. L. Norman, "ZEUS-2D: A Radiation Magnetohydrodynamics Code for Astrophysical Flows in Two Space Dimensions. I. The Hydrodynamic Algorithms and Tests," *Astrophysical Journal Supplement*, vol. 80, p. 753, Jun. 1992.

[56] S. Mirbagheri, H. Bayani, M. Barzegari, and S. Firoozi, *Simulation of Liquid Flow Permeability for Dendritic Structures during Solidification Process*. IntechOpen, 07 2011.

[57] J.-L. Tassoul, *Theory of rotating stars*, ser. Princeton series in astrophysics. Princeton: Princeton University, 1978.

[58] B. Van Leer, "Towards the ultimate conservative difference scheme. iv. a new approach to numerical convection," *Journal of Computational Physics*, vol. 23, no. 3, pp. 276–299, 1977.

[59] J. R. Cash and A. H. Karp, "A variable order runge-kutta method for initial value problems with rapidly varying right-hand sides," *ACM Transactions on Mathematical Software (TOMS)*, vol. 16, no. 3, pp. 201–222, 1990.

[60] W. Press, S. Teukolsky, W. Vetterling, and B. Flannery, *Numerical Recipes: The Art of Scientific Computing*, 3rd ed. Cambridge University Press, 2007.

[61] L. Testi, T. Birnstiel, L. Ricci, S. Andrews, J. Blum, J. Carpenter, C. Dominik, A. Isella, A. Natta, J. P. Williams, and D. J. Wilner, "Dust Evolution in Protoplanetary Disks," in *Protostars and Planets VI*, H. Beuther, R. S. Klessen, C. P. Dullemond, and T. Henning, Eds., Jan. 2014, p. 339.

[62] J. M. Stone and M. L. Norman, "ZEUS-2D: A Radiation Magnetohydrodynamics Code for Astrophysical Flows in Two Space Dimensions. I. The Hydrodynamic Algorithms and Tests," *Astrophysical Journal Supplement*, vol. 80, p. 753, Jun. 1992.

[63] K. R. Bell and D. N. C. Lin, "Using FU Orionis Outbursts to Constrain Self-regulated Protostellar Disk Models," *Astrophysical Journal*, vol. 427, p. 987, Jun. 1994.

[64] Picogna, Giovanni and Kley, Wilhelm, "How do giant planetary cores shape the dust disk? - hl tauri system," *Astronomy & Astrophysics*, vol. 584, p. A110, 2015.

[65] S. J. Weidenschilling, "Aerodynamics of solid bodies in the solar nebula," *Monthly Notices of the Royal Astronomical Society*, vol. 180, no. 2, pp. 57–70, 09 1977.

[66] P. Woitke and C. Helling, "Dust in brown dwarfs. II. The coupled problem of dust formation and sedimentation," *Astronomy and Astrophysics*, vol. 399, pp. 297–313, Feb. 2003.

[67] G. E. Morfill and H. J. Voelk, “Transport of dust and vapor and chemical fractionation in the early protosolar cloud,” *Astrophysical Journal*, vol. 287, pp. 371–395, Dec. 1984.

[68] G. D’Angelo, S. H. Lubow, and M. R. Bate, “Evolution of giant planets in eccentric disks,” *The Astrophysical Journal*, vol. 652, no. 2, p. 1698, dec 2006.